

Final EOARD Report covering the period 1/6/01 to 1/02/02

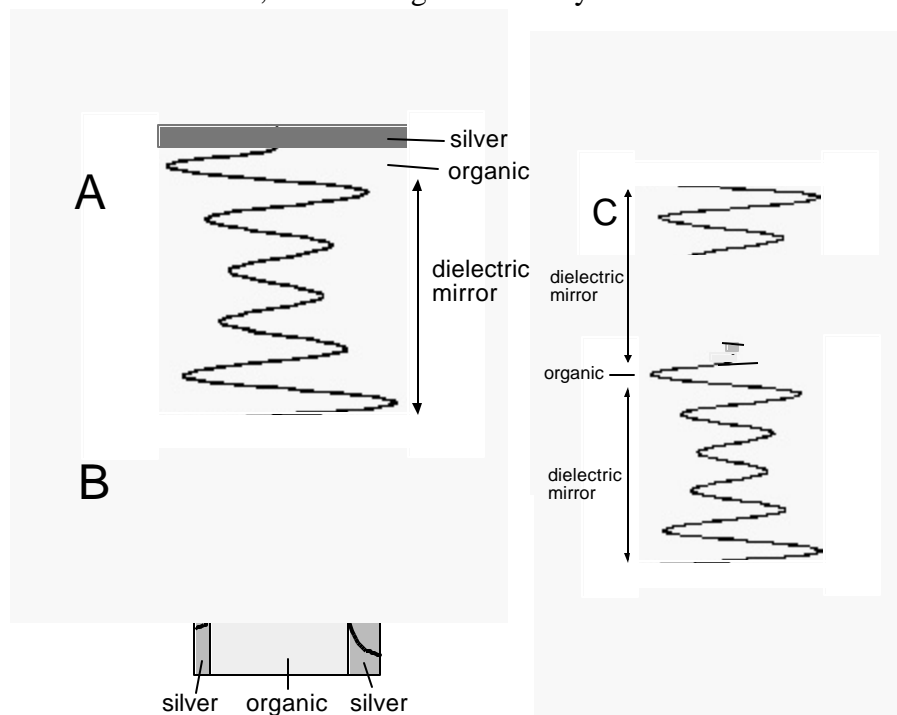
D.G. Lidzey, Department of Physics and Astronomy, The University of Sheffield,
United Kingdom

V.M. Agranovich, Russian Institute for Spectroscopy, Troitsk, Russia,

In the last period of our project, our work has again split into an experimental and theoretical exploration of the properties of strongly coupled organic semiconductor microcavities. We have also worked together in writing a chapter for a book on organic nanostructures, which discusses in detail aspects of the physics of strongly-coupled organic semiconductor microcavities. A copy of this book chapter is included at the end of this report.

A) Experimental Methods and Results

Our experimental work has divided into two distinct areas. Firstly we have explored the fabrication of new types of microcavity containing organic semiconductors. In our previous work, microcavities have been constructed using one high reflectivity dielectric mirror, and one lower reflectivity metallic mirror – structure A. We have now fabricated strongly-coupled microcavities based on two metallic mirrors – structure B, and two high reflectivity dielectric mirrors – structure C below.



Theory indicates that the interaction between a confined optical mode and an excitonic resonance is proportional to the amplitude of the optical field and to the square root of the oscillator strength of the resonance. We have been able to effectively test this idea by constructing microcavities having a significantly enhanced confined optical field amplitude. Structure B is a cavity composed of two metallic (silver) mirrors deposited either side of a thin film of J-aggregates of a cyanine dye. We have previously demonstrated strong-coupling between the cavity photon and the J-aggregate excitons using this material in structures similar to that depicted by structure A. Because the physical cavity

REPORT DOCUMENTATION PAGE

Form Approved OMB No. 0704-0188

Public reporting burden for this collection of information is estimated to average 1 hour per response, including the time for reviewing instructions, searching existing data sources, gathering and maintaining the data needed, and completing and reviewing the collection of information. Send comments regarding this burden estimate or any other aspect of this collection of information, including suggestions for reducing this burden to Washington Headquarters Services, Directorate for Information Operations and Reports, 1215 Jefferson Davis Highway, Suite 1204, Arlington, VA 22202-4302, and to the Office of Management and Budget, Paperwork Reduction Project (0704-0188), Washington, DC 20503.

1. AGENCY USE ONLY (Leave blank)	2. REPORT DATE 1 February 2002	3. REPORT TYPE AND DATES COVERED Final Report	
4. TITLE AND SUBTITLE 'Exciton Hybridisation in Organic-Inorganic Semiconductor Microcavities'		5. FUNDING NUMBERS F61775-00-WE052	
6. AUTHOR(S) Prof. David G. Lidzey			
7. PERFORMING ORGANIZATION NAME(S) AND ADDRESS(ES) University of Sheffield Hicks Bldg., Hounsfield Rd., Sheffield S3 7RH United Kingdom		8. PERFORMING ORGANIZATION REPORT NUMBER N/A	
9. SPONSORING/MONITORING AGENCY NAME(S) AND ADDRESS(ES) EOARD PSC 802 BOX 14 FPO 09499-0200		10. SPONSORING/MONITORING AGENCY REPORT NUMBER SPC 00-4052	
11. SUPPLEMENTARY NOTES			
12a. DISTRIBUTION/AVAILABILITY STATEMENT Approved for public release; distribution is unlimited.		12b. DISTRIBUTION CODE A	
13. ABSTRACT (Maximum 200 words) This report results from a contract tasking University of Sheffield as follows: The contractor will investigate theoretically and experimentally the possibility of hybridizing organic and inorganic semiconductors in microcavities to produce a highly efficient light source that could be either a laser or a very efficient LED. The report describes fabrication of new types of microcavity containing organic semiconductors, including strongly-coupled microcavities based on two metallic mirrors. It further describes development of a theory of cavity polaritons in a disordered organic medium containing J-aggregates.			
14. SUBJECT TERMS EOARD, Organic-inorganic materials, Microcavities, polariton, exciton		15. NUMBER OF PAGES 50	16. PRICE CODE N/A
17. SECURITY CLASSIFICATION OF REPORT UNCLASSIFIED	18. SECURITY CLASSIFICATION OF THIS PAGE UNCLASSIFIED	19. SECURITY CLASSIFICATION OF ABSTRACT UNCLASSIFIED	20. LIMITATION OF ABSTRACT UL

NSN 7540-01-280-5500

Standard Form 298 (Rev. 2-89)
Prescribed by ANSI Std. Z39-18
298-102

length of structure B is much shorter than in structure A, the optical field is effectively concentrated into the organic semiconductor layer. This results in an enhancement of the confined optical field, and thus an enhancement of the interaction between the photons and the excitons. This can be directly measured by an enhanced Rabi-splitting. We measure an enhancement in the Rabi-splitting in the metal-metal cavity of 2.3 times compared to the metal-dielectric mirror cavity. Our theoretical predictions predict a similar enhancement factor. The largest Rabi-splitting that we have observed in such structures is over 330 meV (at room temperature), a value which is extremely large compared to 5 meV measured for gallium arsenide quantum well structures at 10K. Such very strong exciton-photon coupling strengths will be of significant interest in the study of fundamental processes. In particular, we have now achieved the state where the Rabi-splitting energy approaches the binding energy of the organic excitons. We are currently preparing a paper on this work for submission to *Applied Physics Letters*.

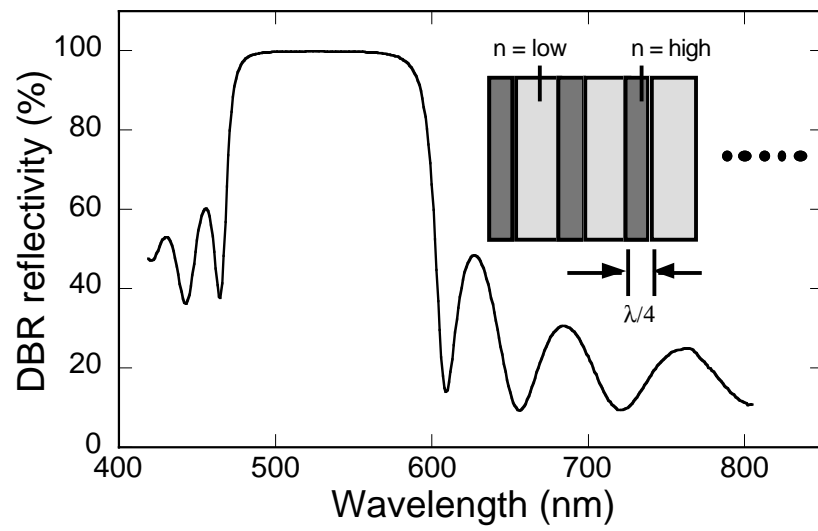
We have now very recently achieved the first strong coupling of organic excitons in microcavities based on two dielectric mirrors (structure C). We have fabricated top dielectric mirrors on the organic layer by thermal evaporation of high (tellurium oxide) and low (lithium fluoride) refractive index dielectrics. This observation is particularly interesting as by using two dielectric mirrors, we will be able to significantly increase the finesse of the microcavity, and create photon states which have much longer confinement times. This will mean that the polariton states in the cavity (the mixed exciton-photon modes) also have a greater lifetime, which will enhance the probability of non-linear scattering processes to be observed. Such scattering processes are currently a topic generating significant excitement in the inorganic semiconductor microcavity community.

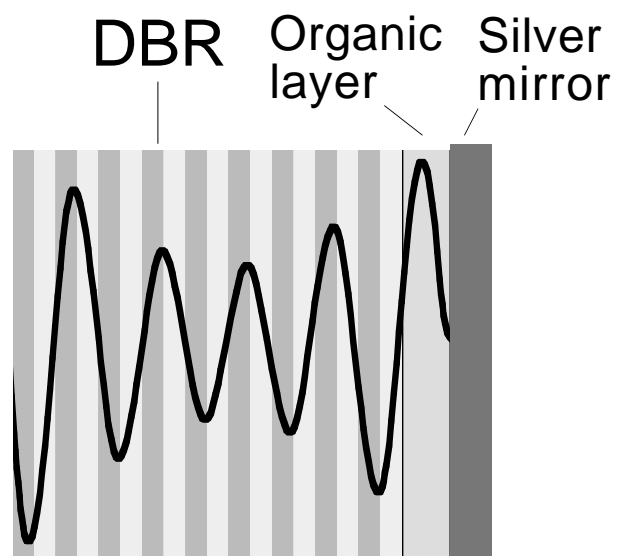
A) Theoretical Methods and Results.

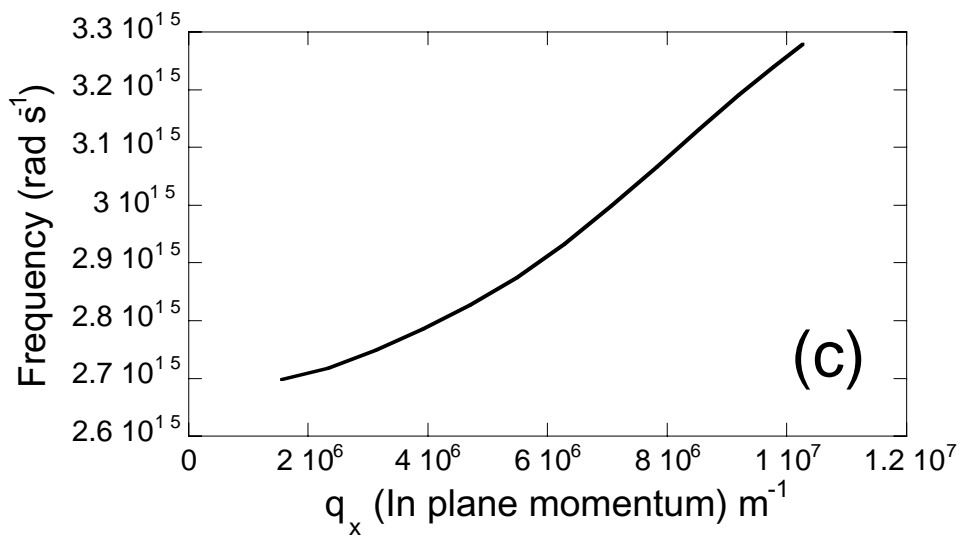
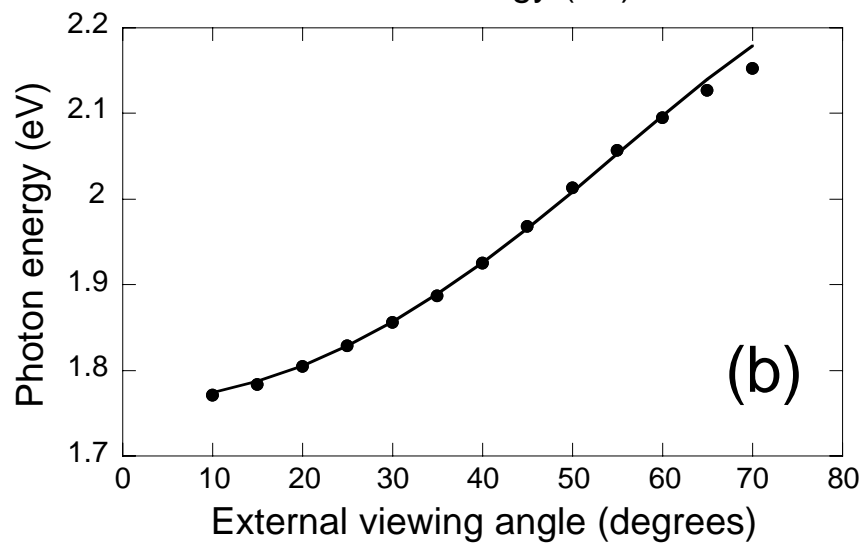
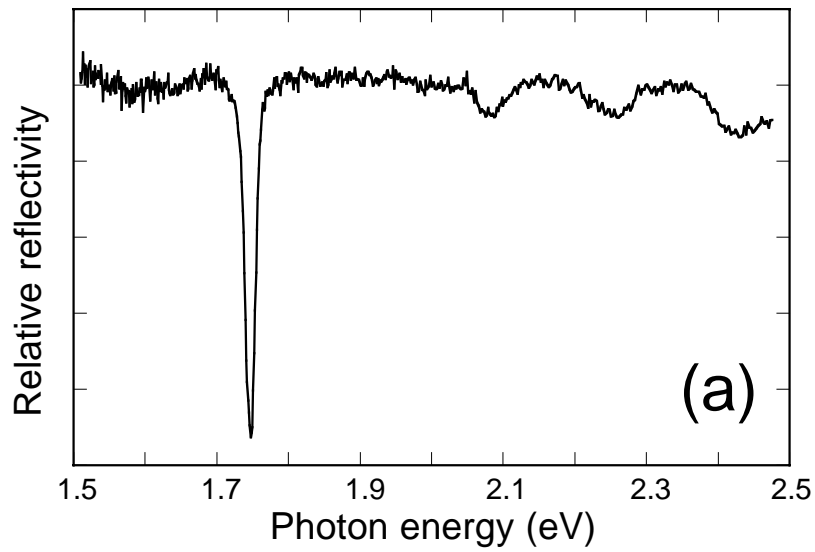
We are developing a theory of cavity polaritons in a disordered organic medium containing J-aggregates. In our macroscopic approach we have confirmed that the resonance in dielectric constant is responsible for the appearance of large (~100 meV) Rabi splittings. This approach will allow to take into account the influence of homogeneous and inhomogeneous broadening of cavity polaritons and such calculations are now in progress. We are also developing a microscopic theory of cavity polaritons in organic microcavities using the Hamiltonian quadratic of the Bose operators of J-aggregate excitons and cavity photons. The main problem with applying this theory to the physical systems produced in the experimental part of the project is to successfully account for the disorder in position and orientation of the different J-aggregates in the cavity. However we have made first steps by averaging over the different J-aggregate positions and orientations *before* we calculate the cavity polariton spectrum. The results of this approach agrees with the result of macroscopic theory where the inhomogeneous broadening is neglected. We have also made a numerical simulation of the organic cavity polariton spectrum. We have found a very unusual inhomogeneous broadening, which we will compare with the experimental data measured from different organic microcavities. This new theoretical direction is very interesting and we plan to investigate a number of different effects which we will compare with experimental data. We attach a draft paper on our theoretical work with this report.

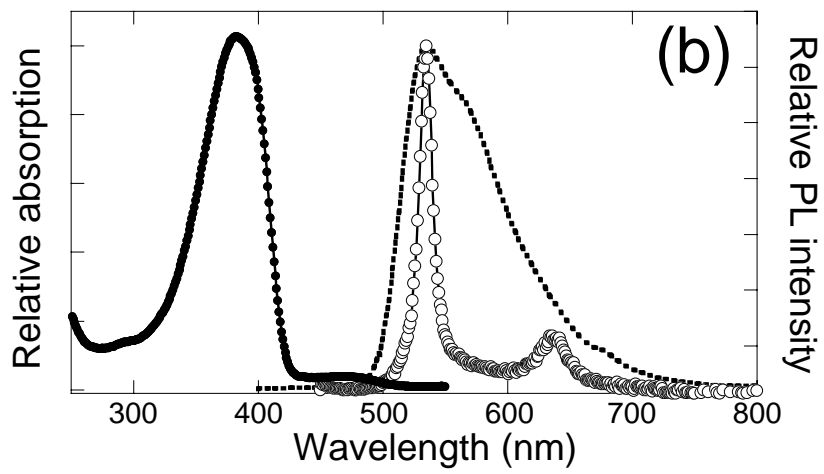
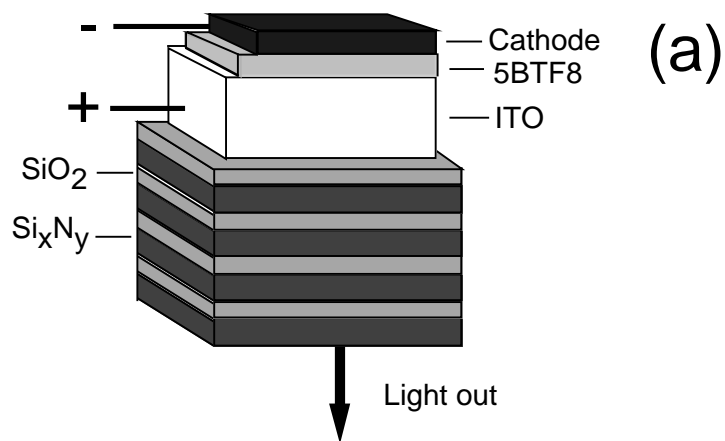
The experimental results have demonstrated that in organic microcavities, the Rabi splitting between the polariton branches can be of the order of 100 meV. This opens new channels for relaxation from the upper polariton branch to the lower branch by the emission of intramolecular optical phonons, having an energy nearly equal to energy of the Rabi splitting. Our microscopic theory discussed above allows us to calculate the rate of this transition. We have found that this rate strongly depends on the optical constants of the J-aggregates and on their concentration in the cavity. For concentrations of the order of 10^{11} to 10^{12} cm⁻² this rate can be of the order of 50 fs. This means that

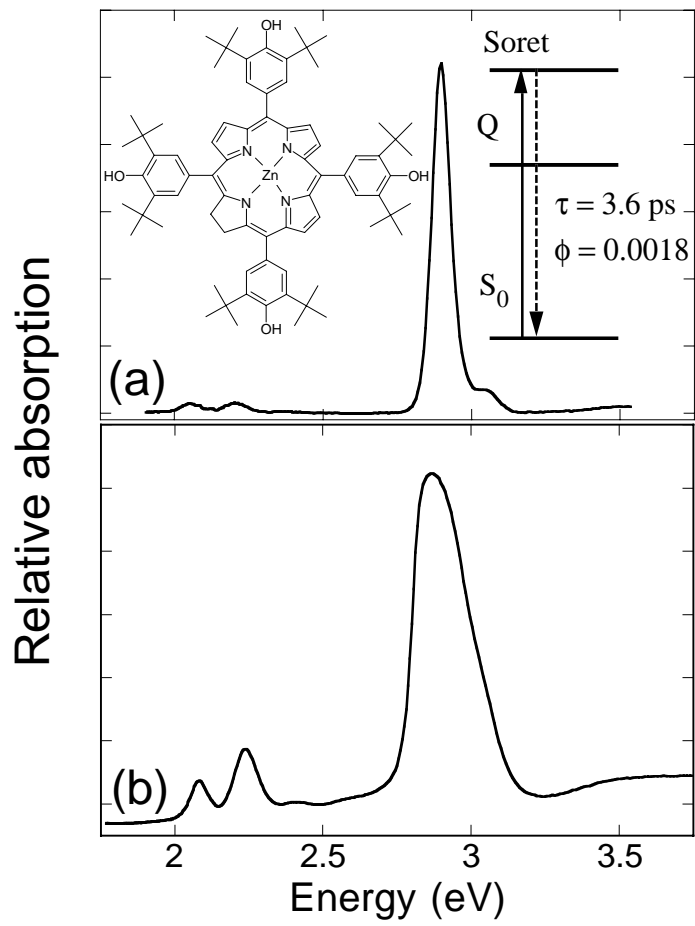
such process can significantly contribute to the population of lower branch cavity polariton states. It is clear that such process may also have an important effect on the spectral distribution of photoluminescence from the microcavity and can be considered as a possible mechanism to create stimulated emission, amplification and organic microcavity polariton lasing. Polariton lasing would require the Bose condensation of cavity polaritons. At present it is not understood whether such effects can be observed experimentally due to the large inhomogeneous broadening of organic cavity polariton states. However we hope that we will be able to address such problems through our joint theoretical and experimental approach.

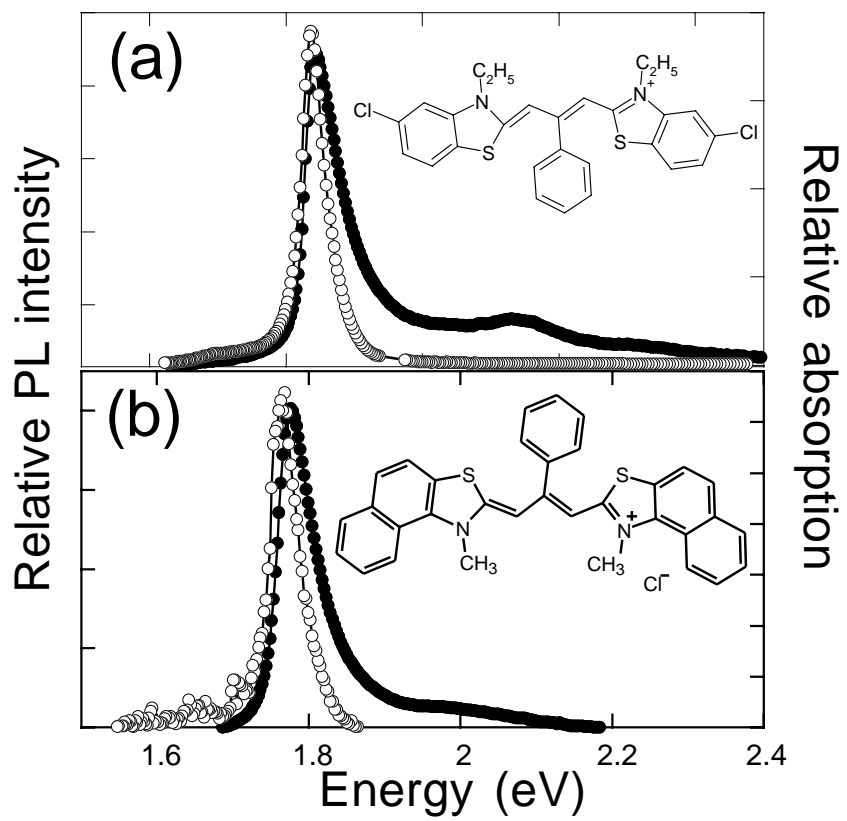


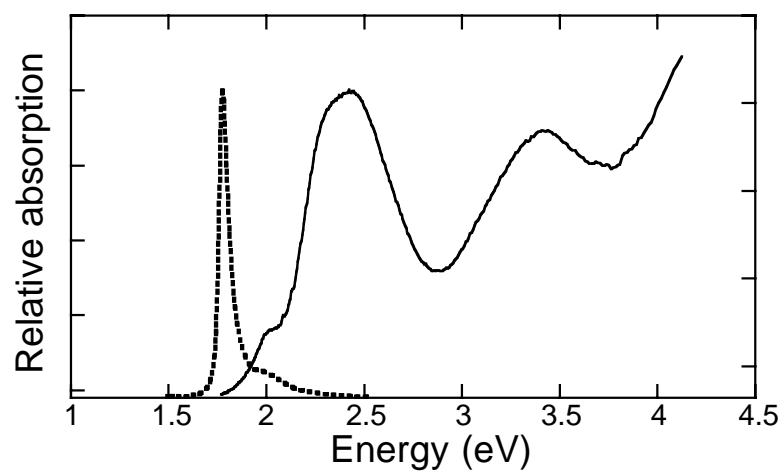




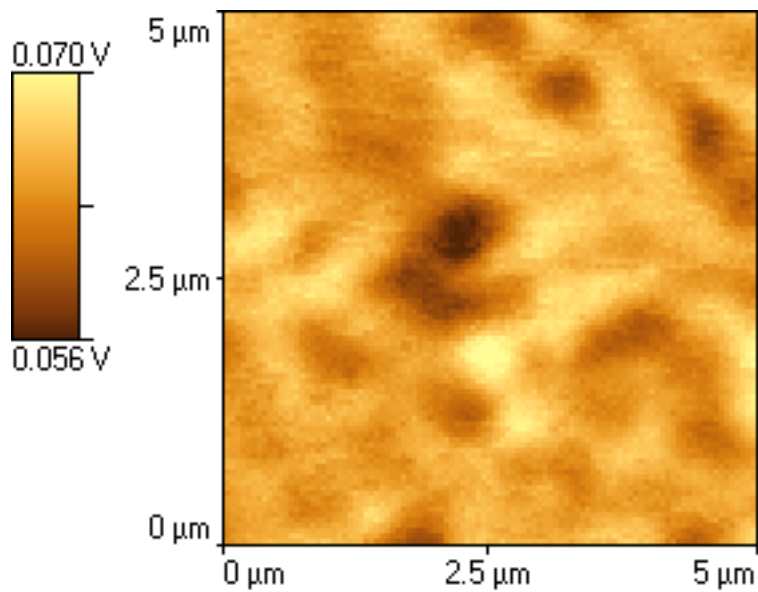




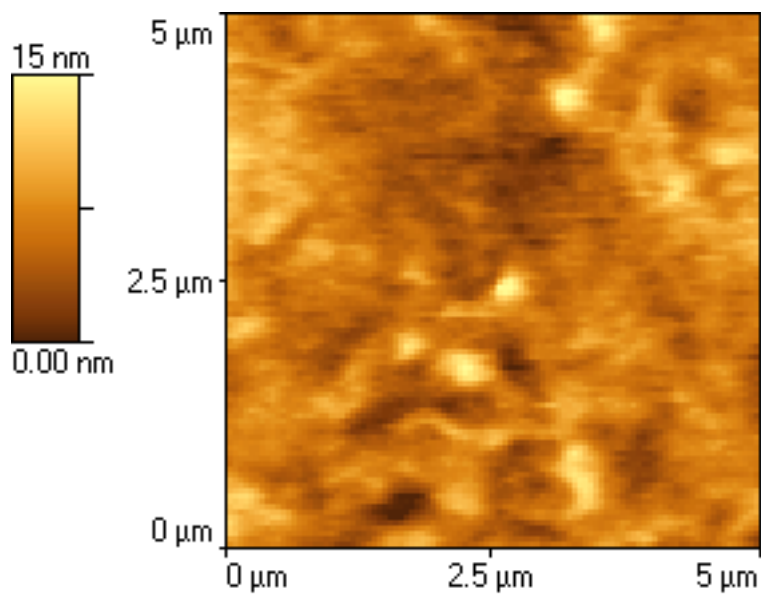


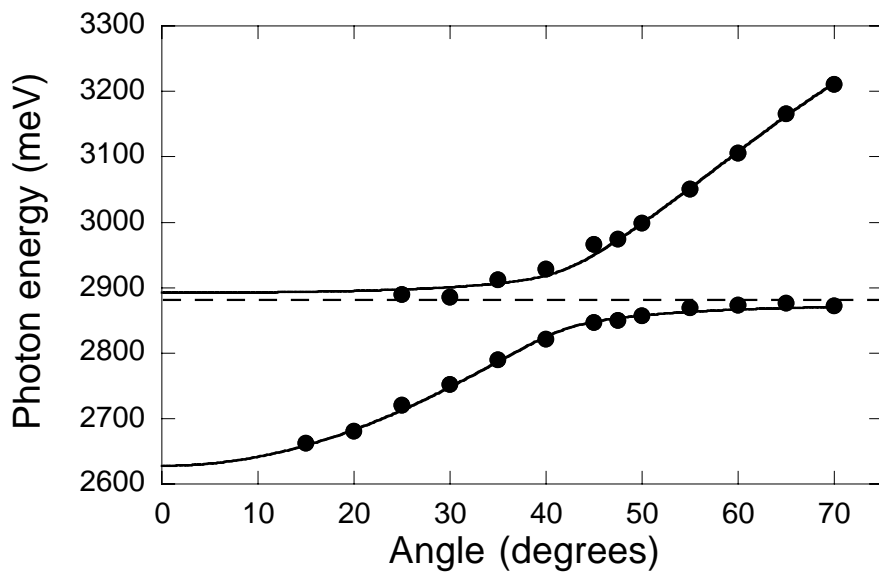


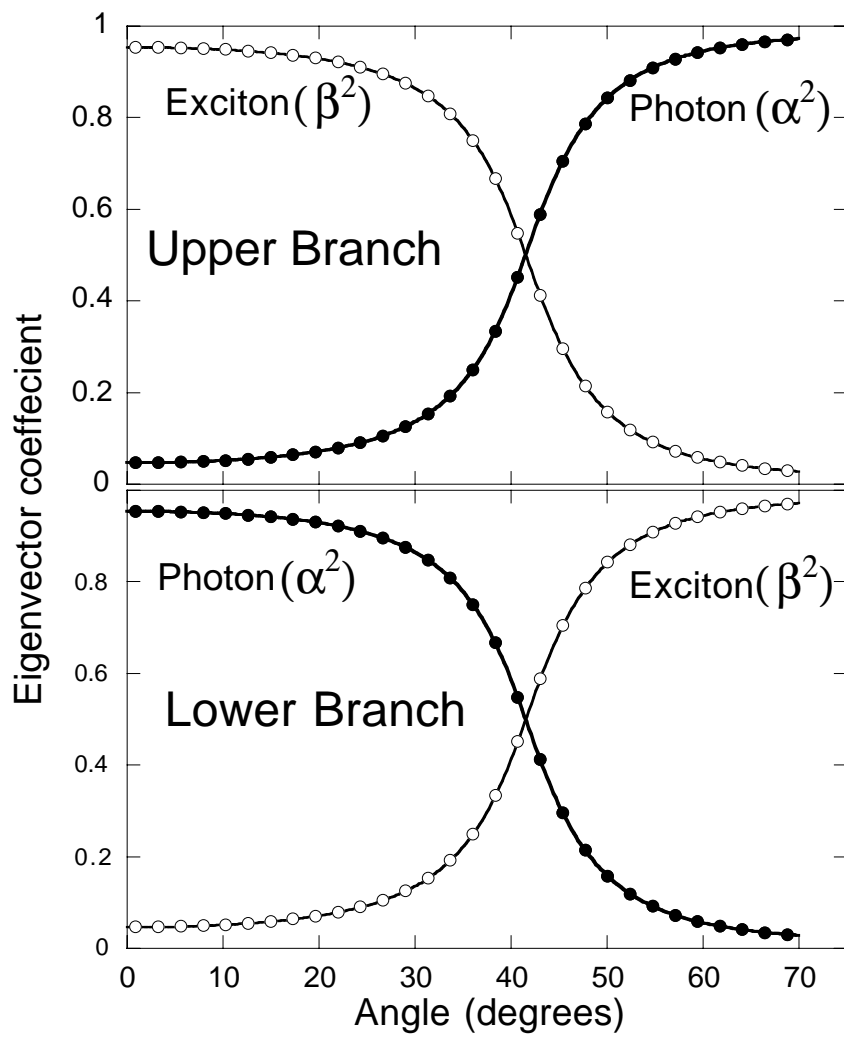
(a): SNOM transmission

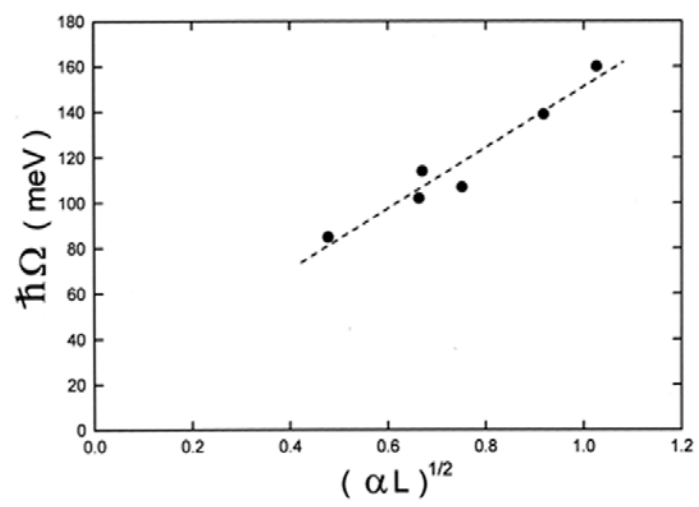


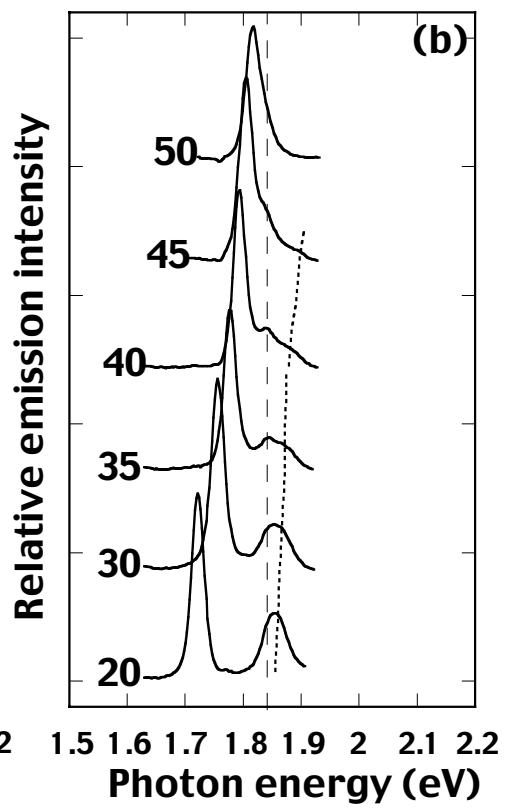
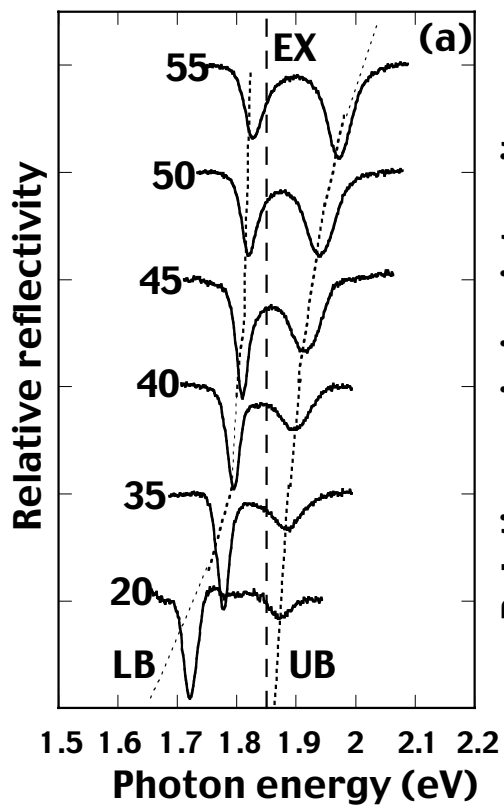
(b): Topography

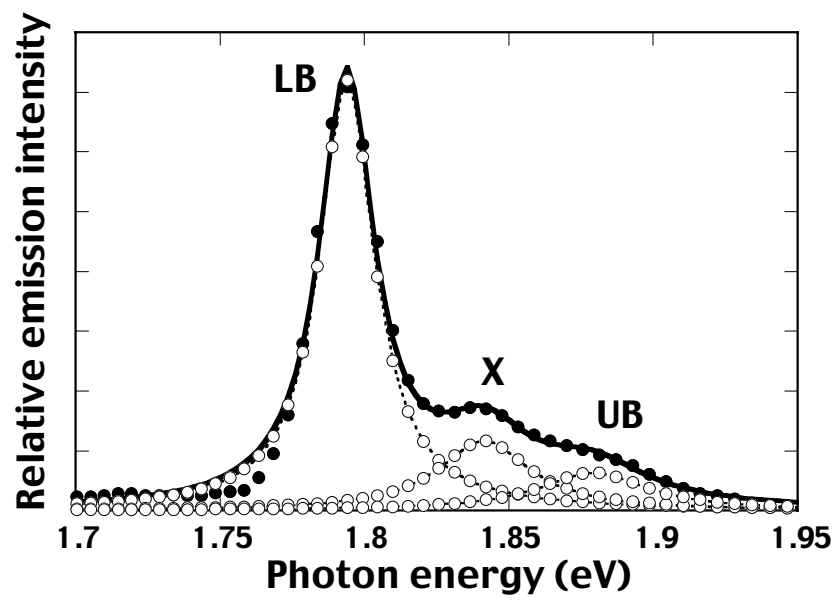


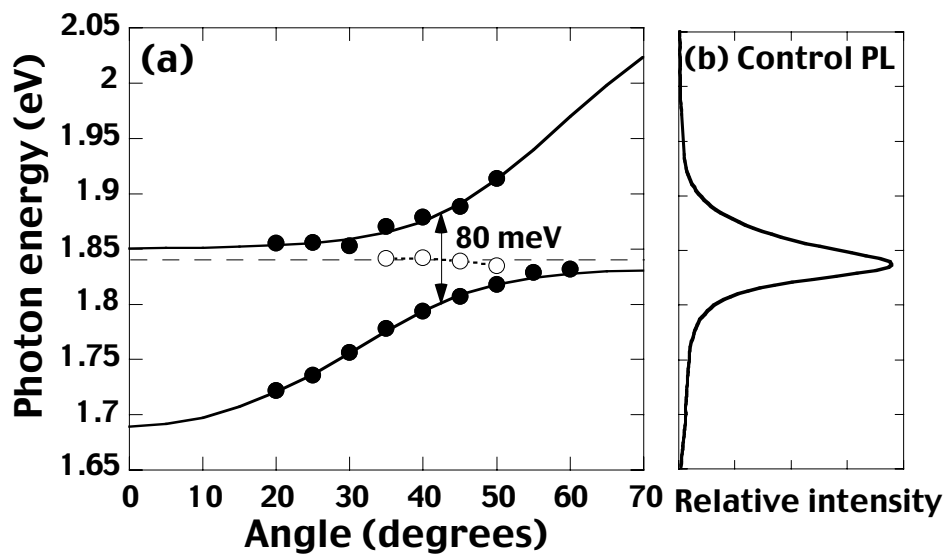


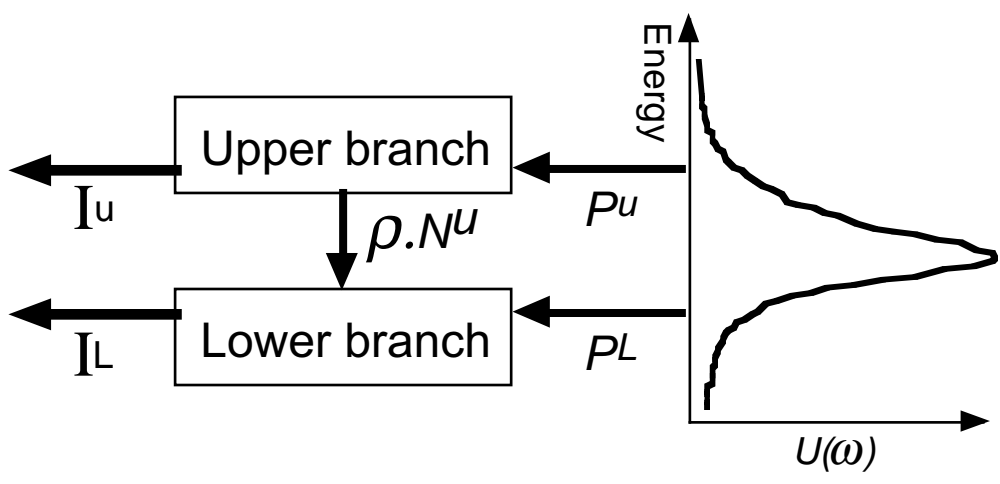


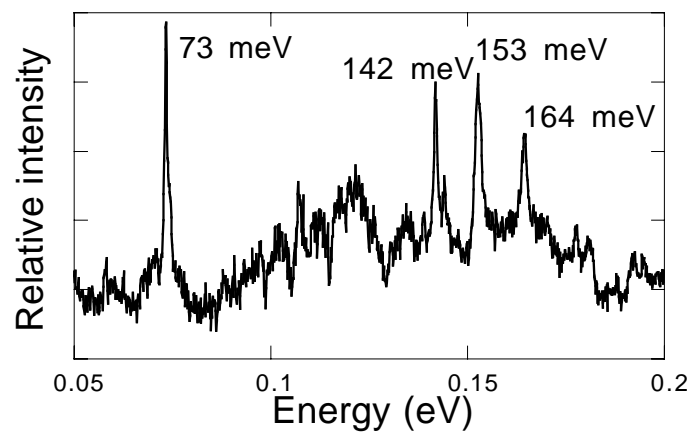


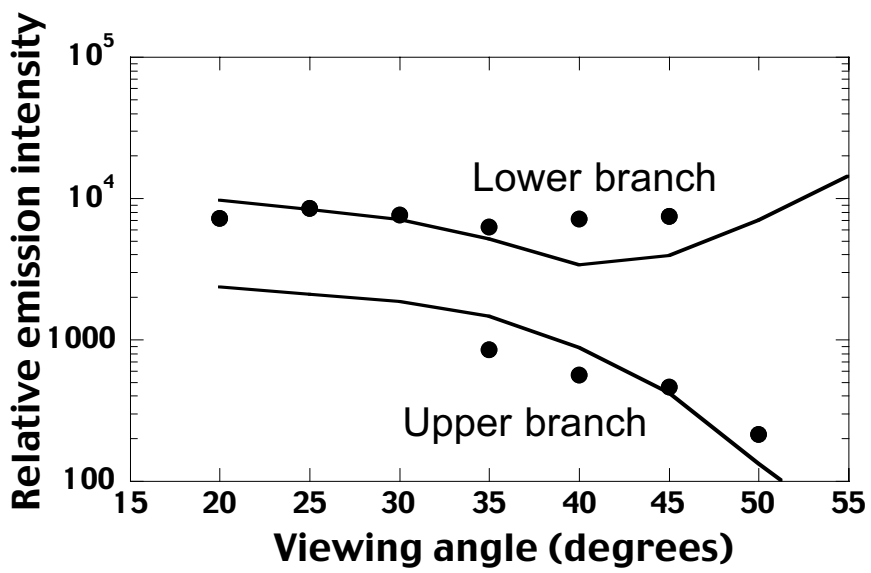


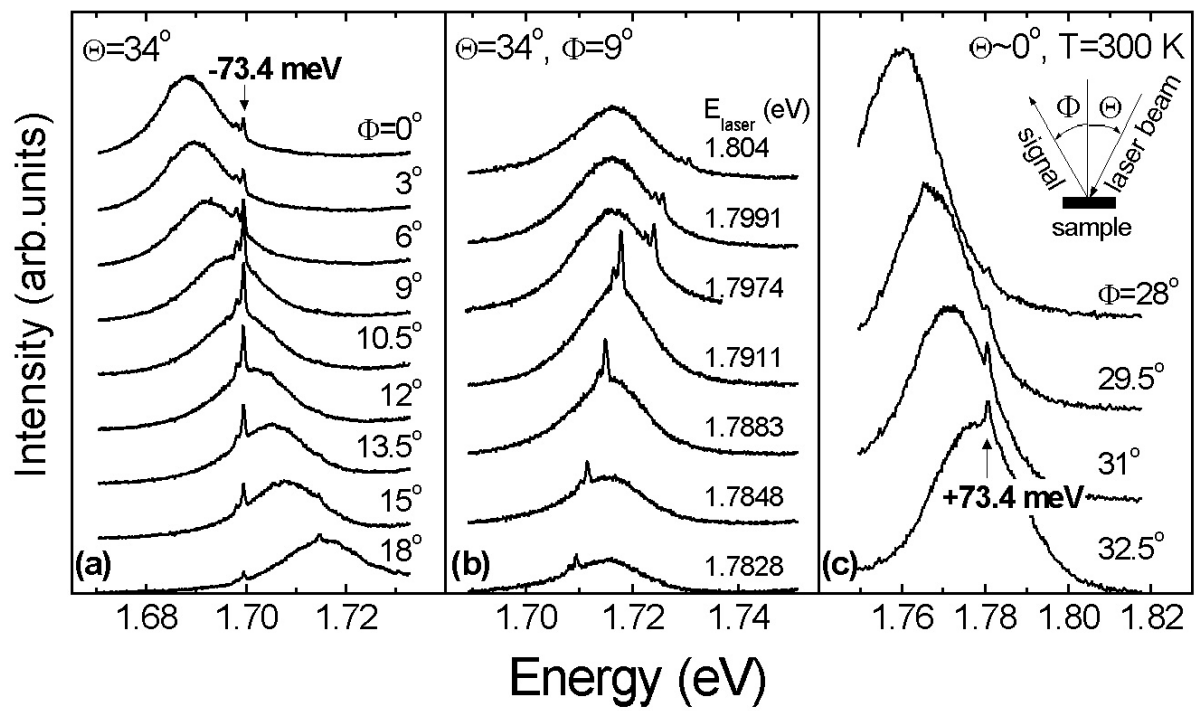


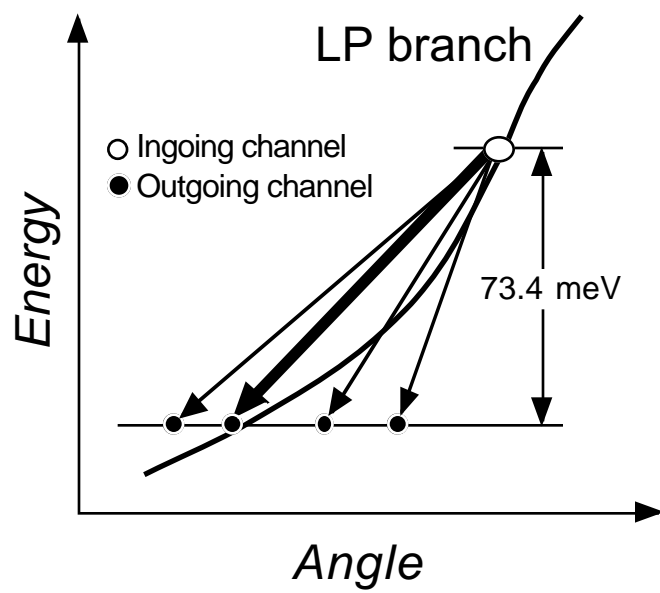


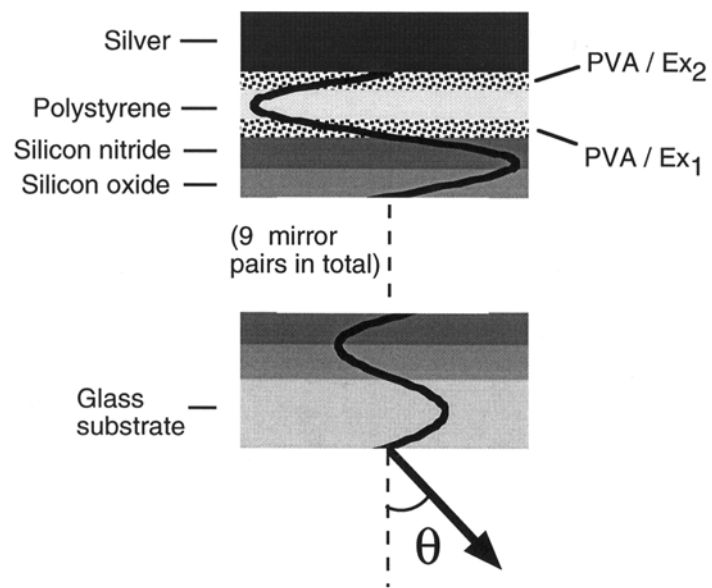


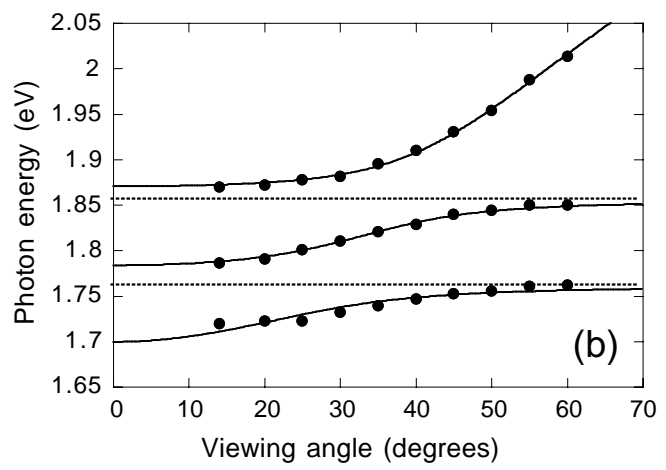
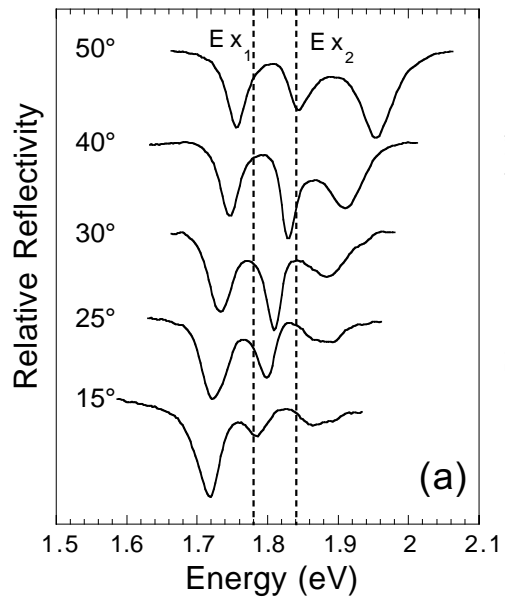












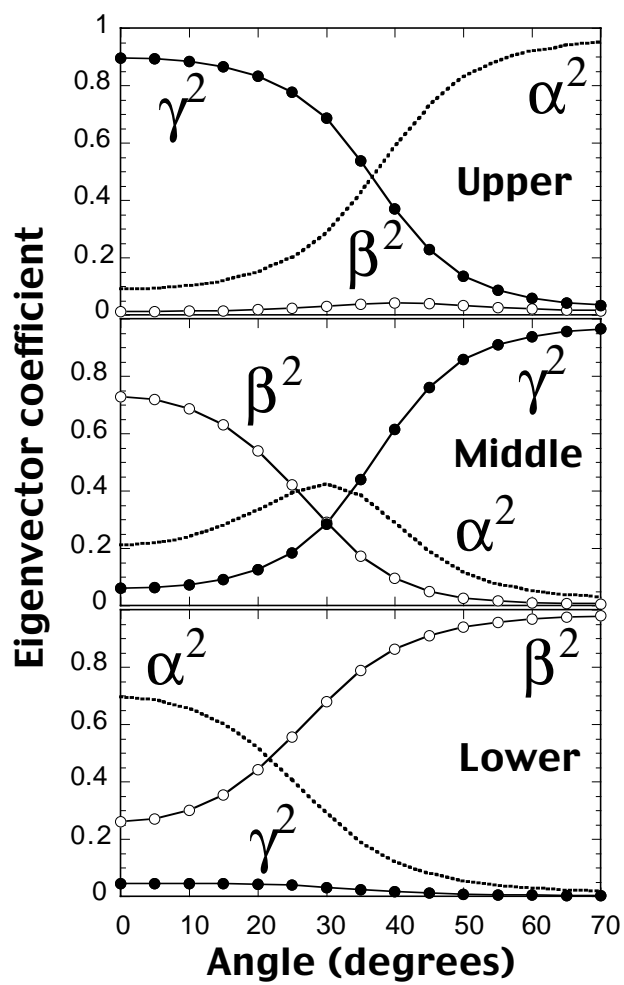


Figure Captions

Figure 1: A schematic diagram of a microcavity, showing the two cavity mirrors and the confined optical field. This particular cavity mode corresponds to an $m = 2$ mode. The internal cavity angle θ_{int} is also defined.

Figure 2: A reflectivity spectrum of a dielectric mirror (DBR) composed of 12 repeat silicon oxide / silicon nitride $\lambda/4$ pairs. The inset shows a schematic diagram of a DBR.

Figure 3: A schematic diagram of a microcavity, composed of a DBR, an organic layer and a silver mirror. The optical field confined by the cavity (calculated using a TMR model) is shown superimposed on the structure.

Figure 4: (a) A reflectivity spectrum measured from a microcavity composed of a DBR, an optically transparent polymer polyvinyl alcohol (PVA), and a silver mirror. The linewidth of the cavity mode is 14 meV. (b) The energy dispersion of the cavity mode as a function of external viewing angle (solid points). The solid line is a calculation of the cavity mode dispersion using equation 2.

Figure 5: (a) Schematic diagram of a resonant cavity LED (RCLED) containing a conjugated polymer as the active charge transporting and emissive material. (b) Absorption (solid dots) and emission (dotted line) from the polymer system used in the RCLED shown in part (a) in a non-cavity device. The spectra shown using open circles is the electroluminescence emission from the RCLED.

Figure 6: (a) The absorption of a thin film of 4TBPPZn molecules in a polystyrene matrix. The insets show the chemical structure of 4TBPPZn, and its energy level scheme. (b) The absorption of a drop-cast film of 4TBPPZn molecules on a quartz substrate.

Figure 7: Absorption (solid dots) and photoluminescence emission (open circles) of a thin film of J-aggregated cyanine dyes in a PVA matrix. Note, the chemical structure of each of the dyes are shown as insets.

Figure 8: The absorption of an amorphous film (solid line) and a J-aggregated film (dotted line) of the cyanine dye shown in figure 7(b).

Figure 9: (a) Transmission scanning near field optical microscope (SNOM) image, and (b) the corresponding shear force image of a thin film of J-aggregates in a PVA matrix.

Figure 10: The experimental setup used to measure both white light reflectivity, and photon emission from an organic semiconductor microcavity. Abbreviations used in this figure: Microcavity (MC), lens (L), Fibre bundle (FB), P (Polarisor).

Figure 11

Figure 12: Dispersion curve measured from a microcavity containing 4TBPPZn molecules. The horizontal dashed line is the peak absorption energy of the 4TBPPZn molecules, about which anticrossing occurs.

Figure 13: Predicted exciton (open dots) and photon (filled dots) coefficients for the upper and lower polariton branches of the cavity whose dispersion curve is shown in figure 12.

Figure 14: The measured Rabi splitting versus the square-root of the peak absorption coefficient measured from cavities containing a thin film of 4TBPPZn molecules in a polystyrene matrix. Note the peak absorption coefficient was determined in each case from an absorption measurement made from a control (non-cavity) film, which had the same thickness and number of 4TBPPZn molecules per cm^3 as were used in the cavity.

Figure 15: (a) Reflectivity spectra measured as a function of angle for a microcavity containing a thin film of the cyanine dye J-aggregates in a PVA matrix, whose absorption and chemical structure are shown in fig 7(a). The dotted lines are a guide for the eye showing the dispersion of the polariton branches. (b) Photoluminescence emission from the cavity as a function of angle following non-resonant optical excitation. The dispersion of the upper polariton branch is shown by a dotted line. In both figures, the peak absorption energy of the J-aggregates are shown by a vertical dashed line.

Figure 16: Photoluminescence emission from the microcavity measured at a viewing angle of 35 degrees. Emission from the upper branch (UB), lower branch (LB) and exciton (X) are clearly identified.

Figure 17: Dispersion curve constructed from the measured photoluminescence emission energy of the cavity shown whose reflectivity and emission spectra are shown in fig 15 (a) and (b). Solid points indicate the measured emission energies, whilst the filled lines are predictions from a model that uses a coupled oscillator model to describe the interaction between the exciton and photon modes. The open circles are the energies of the uncoupled exciton emission (see text for details).

Figure 18: Schematic diagram showing the main components of the model used to describe the emission from the non-resonantly excited microcavity. Here the relative population of the exciton reservoir is plotted as $U(\omega)$. The population of the upper and lower branches is labelled as P (see equation 12), the emission from the branches is labelled as I (see equation 17), and the transfer of population between the branches is labelled as ρ (see equation 13).

Figure 19: Resonant Raman spectrum recorded from the J-aggregated cyanine dye in a PVA matrix used in the microcavity experiments.

Figure 20: Measured photoluminescence emission intensity as a function of angle for the upper and lower polariton branches. Note filled dots are the measured data, whilst the solid lines are the predictions of the model, summarised in equations 18 and 19.

Figure 21: Photoluminescence emission from the microcavity following resonant excitation. In part (a), the excitation angle and energy remains fixed whilst the angle of detection is varies. In part (b), the angles of excitation and emission remain fixed, whilst the energy of excitation is varied. Part (c) shows the room temperature analogue of the data shown in part (a), which were recorded at 120 K. The inset to part (c) defines the angles of excitation and emission.

Figure 22: Schematic diagram of the resonant excitation experiment, illustrating angle tuning. Only when the ingoing (excitation) and outgoing (emission) channels both lie on the lower polariton branch is the condition of exact double resonance achieved.

Figure 23: Schematic diagram of a microcavity containing two different cyanine dyes. Ex_1 corresponds to the dye shown in fig 7(b), and Ex_2 corresponds to the dye shown in fig 7(a).

Figure 24: (a) A series of reflectivity spectra measured at different angles from a microcavity containing two different J-aggregated dyes. The peak absorption energies of the J-aggregates are marked with vertical dashed lines. (b) A dispersion curve of the three polariton branches determined from the spectra shown in part (a). The peak absorption energies of the two J-aggregates around which anticrossing occurs are also shown as horizontal dotted lines.

Figure 25: Predicted exciton and photon coefficients for the upper middle and lower polariton branches of the cavity whose dispersion curve is shown in figure 24 (b). The coefficients α , β and γ correspond to the bare photon, and the Ex_1 and Ex_2 exciton modes respectively. Note in the middle branch at 30 degrees, the state formed is composed of almost equal amplitudes of the photon and the two different excitons.

References

- [Agranovich1] V.M. Agranovich, H. Benisty, C. Weisbuch *Solid State Commun.* **102**, 631-636 (1997).
- [Agranovich2] V.M. Agranovich, G.C. La Rocca, F. Bassani *Phys. Stat. Sol. (a)* **164** 39 (1997)
- [Agranovich3] see “*Spectroscopy and Excitation Dynamics of Condensed Molecular Systems*” Editors V.M.Agranovich and R.M.Hochstrasser, North-Holland, Amsterdam (1983)
- [Alvarado] S.F. Alvarado, P.F. Seidler, D.G. Lidzey, D.D.C. Bradley, *Phys. Rev. Lett.* **81** (5) 1082-1086 (1998)
- [Andrew] P. Andrew, W.L. Barnes, *Science* **290** 785-788 (2000)
- [Anni] M. Anni, G. Gigli, R. Cingolani, S. Patane, A. Arena, M. Allegrini, *Appl. Phys. Lett.* **79** (9) 1382-1384 (2001)
- [Barmy] A. Armitage, D.G. Lidzey, D.D.C. Bradley, T. Virgili, M.S. Skolnick, S. Walker, *Synth. Met.* **111-112** 377-379 (2000)
- [Barmy2] A. Armitage, M.S. Skolnick, A.V. Kavokin, D.M. Whittaker, V.N. Astratov, G.A. Gehring, J.S. Roberts *Physical Review B* **58** (23) 15367-15370 (1998)
- [Barmy3] A. Armitage, M.S. Skolnick, V.N. Astratov, D.M. Whittaker, G. Panzarini, L.C. Andreani, T.A. Fisher, J.S. Roberts, A.V. Kavorkin, M.A. Kaliteevski, M.R. Vladimirova, *Phys. Rev. B* **57** (23) 14877-14881 (1998)
- [Barnes] P.T. Worthing, J.A.E. Wasey, W.L. Barnes, *J. Appl. Phys.* **89** (1) 615-625 (2001)
- [Basko] D.M. Basko, F. Bassani, G.C. La Rocca, V.M. Agranovich, *Phys. Rev. B.* **62** (23) 15962-15977 (2000)
- [Book] L.D. Book, N.F. Scherer, *J. Chem. Phys.* **111** (3) 792-795 (1999)
- [Bos] F. Bos, *Appl. Optics* **20**, 1886 (1981).
- [Boudon] G. Bourdon, I. Robert, R. Adams, K. Nelep, I. Sagnes, J.M. Moison, I. Abram, *Appl. Phys. Lett.* **77** (9) 1345-1348 (2000)
- [Bradley] A.L. Bradley, J.P. Doran, T. Aherne, J. Hegarty, R.P. Stanley, R. Houdre, U. Oesterle, M. Ilegems, *Phys. Rev. B* **57** (16) 9957-9964 (1998)
- [Burns] S.E. Burns, N. Pfeffer, J. Gruner, M. Remmers, T. Javoreck, D. Neher, R.H. Friend, *Adv. Mater.* **9** (5) 395-398 (1997)
- [Cimrova] V. Cimrova, U. Scherf, D. Nehr, *Appl. Phys. Lett.* **69** (5) 608-610 (1996)

[Dang] Le Si Dang, D. Heger, R. Andre, F. Boeuf, R. Romestain, *Phys. Rev. Lett.* **81** (18) 3920-3923 (1998)

[Denton] G.J. Denton, N. Tessler, M.A. Stevens, S.E. Burns, N.T. Harrison, R.H. Friend, *Proceedings of the SPIE*, **3145** 24-35 (1997)

[Ell] C. Ell, J. Prineas, T.R. Nelson, S. Park, H.M. Gibbs, G. Khitrova, S.W. Koch, R. Houdre, *Phys. Rev. Lett.* **80**, 4795 (1998)

[Era] M. Era, S. Morimoto, T. Tsutsui, S. Saito, *Appl. Phys. Lett.* **65** (6) 676-678 (1994)

[Fainstain1] A. Fainstain, B. Jusserande, V. Thierry-Mieg, *Phys. Rev. Lett.* **75**, 3764-3767 (1995)

[Fainstain2] A. Fainstain, B. Jusserand, V. Thierry-Mieg, *Phys. Rev. Lett* **78** 1576-1579 (1997)

[Fainstain3] A. Fainstain, B. Jusserand, *Phys. Rev. B* **57** 2402 (1997)

[Fisher] T.A. Fisher, D.G. Lidzey, M.A. Pate, M.S. Weaver, D.M. Whittaker, M.S. Skolnick, D.D.C. Bradley, *Appl. Phys. Lett.* **67** (10) 1355-1358 (1995)

[Fleming] G.R. Fleming, R. van Grondelle *Physics Today* 48-55 (February 1994)

[Fletcher] R.B. Fletcher, D.G. Lidzey, D.D.C. Bradley, M. Bernius, S. Walker, *Appl. Phys. Lett.* **77** (9) 1262-1264 (2000)

[footnote] This time is twice the cavity escape time, as at resonance each polariton can be thought of as 'spending' half its time as a photon, and half its time as an exciton. As escape only occurs during its photon-like part of its cycle, the polariton lifetime is approximately twice that of a cavity photon.

[Fujita] T. Fujita, Y. Sato, T. Kuitana, T. Ishihara, *Phys. Rev. B* **57** (19) 12428-12434 (1998)

[Ginger] Finlayson CE, Ginger DS, Greenham NC, *Chem. Phys. Lett.* **338** (2-3) 83-87 (2001)

[Hecht] see E. Hecht "Optics" 2nd Edition, Addison-Wesley Pubs. Chapter 9 (1987)

[Ho] P.K.H. Ho, D.S. Thomas, R.H. Friend, N. Tessler *Science* **285** 233-236 (1999)

[Hopmeier1] M. Hopmeier, U. Siegner, U. Lemmer, W. Guss, J. Pommerehne, R. Sander, A. Greiner, R.F. Mahrt, H. Bassler, J. Feldmann, E.O. Gobel, *Synth Met.* **76** (1-3) 117-119 (1996)

[Hopmeier2] M. Hopmeier, W. Guss, M. Deussen, E.O. Gobel, R.F. Mahrt, *Phys. Rev. Lett.* **82** (20) 4118-4121 (1999)

[Houdre] R. Houdré, R.P. Stanley, U. Oesterle, P. Pellandini, M. Ilegemes, "Microcavities and Photonic Bandgaps: Physics and Applications" Editors J. Rarity & C. Weisbuch, NATO ASI Series E: Applied Sciences – vol 324, pg 33-42, Kluwer Academic press (1996)

[Houdre2] R. Houdré, C. Weisbuch, R.P. Stanley, U. Oesterle, P. Pellandini, M. Ilegemes, *Phys. Rev Lett.* **73** 15 2043-2046 (1994)

- [Huang] R. Huang, F. Tassone, Y. Yamamoto, *Phys. Rev. B* **61** (12) R7854 (2000)
- [Jordan] R.H. Jordan, L.J. Rothberg, A. Dodabalapur, R.E. Slusher, *Appl. Phys. Lett.* **69** (14) 1997-1999 (1996)
- [Knapp] E.W. Knapp, *Chem. Phys.* **85** 73-82 (1984)
- [Kobayashi] T. Kobayashi (Ed.), "J-Aggregates" (World Scientific) Singapore (1996).
- [Lidzey1] D.G. Lidzey, D.D.C. Bradley, M.S. Skolnick, T. Virgili, S. Walker, D.M. Whittaker, *Nature* **395** 53 (1998)
- [Lidzey2] D.G. Lidzey, D.D.C. Bradley, T. Virgili, A. Armitage, M.S. Skolnick, S. Walker *Phys. Rev. Lett.* **82** (16) 3316-3319 (1999)
- [Lidzey3] D.G. Lidzey, D.D.C. Bradley, A. Armitage, S. Walker, M.S. Skolnick, *Science* **288** 1620-1623 (2000)
- [Lidzey4] D.G. Lidzey, D.D.C. Bradley, S.J. Martin, M.A. Pate, *IEEE Journal of Selected Topics in Quantum Electronics* **4** (1) 113-118 (1998)
- [Lidzey5] T. Virgili, D.G. Lidzey, M. Grell, S. Walker, A. Asimakis, D.D.C. Bradley, *Chem. Phys. Lett.* **341** 219-224 (2001)
- [Lidzey6] D.G. Lidzey, D.D.C. Bradley, M.A. Pate, J.P.R. David, D.M. Whittaker, T.A. Fisher, M.S. Skolnick, *Appl. Phys. Lett.* **71** (6) 744-746 (1997)
- [Lidzey7] D.G. Lidzey, D.D.C. Bradley, M.S. Skolnick, S. Walker, *Synth. Met.* **124** 37-40 (2001)
- [Lidzey8] D.G. Lidzey, A.M. Fox, M.D. Rahn, M.S. Skolnick, V.M. Agranovich, S. Walker, *Submitted to Phys. Rev. B* (2002)
- [Mobius] D. Möbius *Advanced Materials* **7** (5) 437-443 (1995)
- [Muller] M. Muller, J. Bleuse, R. Andre, *Phys. Rev. B* **62** (24) 16886-16892 (2000)
- [Norris] T.B. Norris, *Confined Electrons and Photons*, pg 503-521 Eds. E. Burstein & C. Weisbuch, Plenum Press, New York (1995)
- [Norris2] T.B. Norris, J.K. Rhee, C.Y. Sung, Y. Arakawa, M. Nishioka, *Phys. Rev.* **B50** (19) 14633-14666 (1994)
- [Piron] R. Piron, E. Toussaere, D. Josse, J. Zyss, *Appl. Phys. Lett.* **77** (16) 2461-2463 (2000)
- [Porphyrin] *The Porphyrins*, D. Dolphin Ed (Academic Press, New York, 1978)
- [Potma] E.O. Potma, D.A. Wiersma, *J. Chem. Phys.* **108**, 4894 (1998)

- [Saba] M. Saba, C. Ciuti, J. Bloch, V. Thierry-Mieg, R. Andre, Le Si Dang, S. Kundermann, A. Mura, G. Bongiovanni, J.L. Staehli, B. Deveaud, *Nature* XXXX (2001)
- [Sasha] A.I. Tartakovskii, M. Emam-Ismael, D.G. Lidzey, M.S. Skolnick, D.D.C. Bradley, S. Walker, V.M. Agranovich, *Phys. Rev. B* **63** 121302(R) (2001)
- [Sasha2] A.I. Tartakovskii, M. Emam-Ismael, R.M. Stevenson, M.S. Skolnick, V.N. Astratov, D.M. Whittaker, J.J. Bamberg, J.S. Roberts, *Phys. Rev. B* **62** (4) R2283-R2286 (2000)
- [Savona] V. Savona, C. Weisbuch, *Phys. Rev. B* **54** (15) 10835-10840 (1996)
- [Savvidis] P.G. Savvidis, J.J. Baumberg, R.M. Stevenson, M.S. Skolnick, D.M. Whittaker, J.S. Roberts, *Phys. Rev. Lett.* **84** 1547 (2000)
- [Savvidis2] P.G. Savvidis, J.J. Baumberg, R.M. Stevenson, M.S. Skolnick, D.M. Whittaker, J.S. Roberts, *Phys. Rev. B* **62** (20) R13278 (2000)
- [scattering]
- [Schouwink] P. Schouwink, H.V. Berlepsch, L. Dahne, R.F. Mahrt, *Chem. Phys. Lett.* **344** 352-356 (2001)
- [Sermage] B. Sermage, S. Long, I. Abram, J.Y. Marzin, J. Bloch, R. Planel, V. Thierry-Mieg, *Phys. Rev.* **B53** 16516 (1996)
- [Shkunov] M.N. Shkunov, W. Gellermann, Z.V. Vardeny, *Appl. Phys. Lett.* **73** (20) 2878-2880 (1998)
- [Skolnick] M.S. Skolnick, T.A. Fisher, D.M. Whittaker, *Semicond. Sci. Technol.* **13**, 645-669 (1998)
- [Stanley1] R.P. Stanley, R. Houdre, U. Oesterle, M. Gailhanou, M. Ilegems, *Appl. Phys. Lett.* **65** (15) 1883-1885 (1994)
- [Stanley2] R.P. Stanley, S. Pau, U. Oesterle, R. Houdré, M. Ilegems, *Phys. Rev.* **B55** R4867 (1997)
- [Stanley3] R.P. Stanley, R. Houdré, C. Weisbuch, U. Oesterle, M. Ilegems, *Phys. Rev.* **B 53**, 16 10995-11007 (1996)
- [Stevenson] R.M. Stevenson, V.N. Astratov, M.S. Skolnick, D.M. Whittaker, M. Emam-Ismael, A.I. Tartakovskii, P.G. Savvidis, J.J. Baumberg, J.S. Roberts, *Phys. Rev. Lett* **85** (17) 3680-3686 (2000)
- [Sturmer] D.M. Sturmer and D.M. Heseltine, in "The theory of photographic processes" ed. T.H. James (Macmilan Publishing Co.) New York (1977)
- [Tsutsui] K. Sumioka, H. Nagahama, T. Tsutsui, *Appl. Phys. Lett.* **78** 1328 (2001)
- [Unlu] Ünlü, M.S., Strite, S. *J.Appl.Phys.* **78**, 607-638 (1995)
- [Vredenberg] A.M. Vredenberg, N.E.J. Hunt, E.F. Schubert, D.C. Jacobson, J.M. Poate, G.J. Zydzik, *Phys. Rev. Lett.* **71** (4) 517-520 (1993)

[Wainstain1] J. Wainstain, C. Delalande, D. Gendt, M. Voos, J. Bloch, V. Thierry-Mieg R. Planel *Physical Review B* **58** (11) 7269-7279 (1998)

[Wainstain2] J. Wainstain, G. Cassabois, PH. Roussignol, C. Delalande, M. Voos, F.T. Assone, R. Houdré, R.P. Stanley, U. Oesterle, *Superlattices and Microstructures* **22**, 3, 389-392 (1997)

[Wainstain3] J. Wainstain, C. Delalande, M. Voos, R. Houdré, R.P. Stanley, U. Oesterle, *Solid State Communications*, **99**, 5, 317-321 (1996)

[Wainstain4] J. Wainstain, C. Delalande, M. Voos, J. Bloch, V. Thierry-Mieg, R. Planel, R. Houdré, R.P. Stanley, U. Oesterle, *Solid State Communications*, **106**, 11, 711-714 (1998)

[Weisbuch] C. Weisbuch, M. Nishioka, A. Ishikawa, Y. Arakawa, *Phys. Rev. Lett.* **69** 3314-3318 (1992)

[Weisbuch2] C. Weisbuch, H. Benisty, R. Houdre, *Journal of Luminescence* **85** 271-293 (2000)

[Zhu] Y. Zhu, D.J. Gauthier, S.E. Morin, Q. Wu, H.J. Carmichael, T.W. Mossberg, *Phys. Rev. Lett.* **64** (21) 2499-2502 (1990)

Strong Optical Coupling in Organic Semiconductor Microcavities

David G. Lidzey

Contents

- 1.1 Introduction
- 1.2 Organic Semiconductor Microcavities
 - 1.2.1 The Optical Properties of Microcavities
 - 1.2.2 Weak Coupling
 - 1.2.3 Strong Coupling
- 1.3 Organic Semiconductors for Strong Optical Coupling
 - 1.3.1 Background
 - 1.3.2 Molecular Dyes
 - 1.3.3 J-Aggregates and other Self Assembled Systems
- 1.4 Optical Measurement Techniques
- 1.5 Dispersion of Cavity Polaritons
 - 1.5.1 Reflectivity Measurements of Strongly-Coupled Cavities
 - 1.5.2 Macroscopic and Microscopic Analysis of Dispersion
- 1.6 Cavity Emission Following Non-Resonant laser Excitation
 - 1.6.1 Experimental Observations
 - 1.6.2 A Model for Non-Resonant Excitation and Emission
- 1.7 Photon Emission Following Resonant Excitation
 - 1.7.1 Resonant Excitation Measurements
 - 1.7.2 The Generation of Raman Emission in a Microcavity
- 1.8 Photon-Mediated Hybridisation between Frenkel Excitons
 - 1.8.1 Hybrid Semiconductor Microcavities
- 1.9 Future Prospects
- Appendix
- References

1.1 Introduction

A semiconductor microcavity is a structure in which a wavelength-thickness semiconductor layer is positioned between two closely separated mirrors. The cavity mirrors quantize the local electromagnetic field into a set of discrete confined photon modes. If the energy of one of the modes is resonant with an optical transition of the semiconductor, it is possible to modify both the semiconductor absorption and emission characteristics. Such structures are of fundamental and practical interest, with applications in lasers and other light-emitting devices [Fletcher, Unlu, Ho, Saba, Jordan, Piron, Lidzey4].

There are two regimes into which the interactions between a semiconductor and the electromagnetic field can be classified, namely the weak and strong-coupling regimes. In the strong-coupling regime, a cavity photon couples to an exciton having the same energy and in-plane momentum. The coherent coupled state thus formed is termed a cavity-polariton, and can be considered as an admixture of the exciton and cavity-photon modes. Strong-coupling in microcavities was first observed in 1994 by Weisbuch and colleagues, who fabricated

heterostructures containing a series of inorganic (III-V) quantum-wells (QWs) [Weisbuch]. Since then strongly-coupled inorganic semiconductor microcavities have been extensively studied both experimentally [Skolnick, Norris, Weisbuch2] and theoretically [Zhu] by a large number of groups. The reader who wishes to delve deeper into the subject of optical strong coupling in microcavities, is encouraged to consult a number of comprehensive review papers listed at the end of this chapter [refs]. Even though the subject has now reached a degree of maturity, the observation of new effects in strongly-coupled microcavities continues to surprise and delight researchers. One important advance that has emerged within the past few years has been the observation that organic semiconductors can also undergo strong-coupling in suitably designed optical resonators. This advance is particularly important if strong-coupling is to find applications, as the binding energy of organic (Frenkel) excitons in conjugated polymers is usually between 0.1 and 0.5 eV [Alvarado], and of the order of 1 eV in molecular crystals [Pope]. This allows the direct observation and manipulation of Frenkel excitons at room temperature. This is in contrast to inorganic (Mott-Wannier) quantum-well excitons, whose binding energy is typically around 10 meV (dependent on well-width and barrier composition), which thus requires the use of low temperatures to facilitate their observation.

In this chapter, we review our research on strong-coupling in microcavities using organic semiconductors. In section 1.2 we discuss the optical properties of microcavities both in the weak and strong-coupling regimes. In section 1.3, we summarise the requirements that a semiconductor material must possess to undergo strong-coupling in a microcavity, and discuss the optical properties of a number of organic materials that we have used to achieve strong coupling. In section 1.4 we summarise the experimental methods that we have used to study such structures. Section 1.5 presents some of our observations made via white light reflectivity measurements, whilst in section 1.6 and 1.7, the photon emission from organic strongly-coupled microcavities is presented following both non-resonant and then resonant excitation respectively. In section 1.8, we present our results on microcavities containing two different organic semiconductors, and demonstrate how such structures support new types of hybridised and delocalised optical excitations. Finally, in section 1.9 we outline the possible future developments and applications that may emerge from this exciting research area.

1.2 Organic Semiconductor Microcavities.

1.2.1 The Optical Properties of Microcavities

A microcavity is a planar Fabry-Perot cavity in which two mirrors are placed either side of a dielectric medium. The presence of the two mirrors quantizes the cavity photon modes, such that only photons having a certain energy and in-plane momentum can be supported. Such photons are confined by the cavity until they either escape from the cavity by penetration through one of the mirrors, or until some optical loss mechanism occurs, such as scattering or absorption. For the simplest case of two infinitely reflecting mirrors (fig 1) a series of cavity modes are supported having a wavelength λ measured outside the cavity given by the expression

$$\frac{m\lambda}{2} = nL \cos q_{\text{int}} \quad (1)$$

where m is a mode number, n is the refractive index of the medium between the mirrors and L is their physical separation. In this equation, we have the usual definition of wavelength

$$l = \frac{2pc}{\omega} \quad (2)$$

where ω is the angular frequency of light, and c is the speed of light in vacuum. The frequency of the cavity mode is dependent on its in-plane wavevector. The in-plane wavevector of the cavity mode (q_x^{cav}) determines the angle at which it is detected from outside the cavity. The in-plane wavevector of a cavity mode corresponding to an angle θ_{int} is given by

$$q_x^{cav} = \frac{\omega n}{c} \sin \mathbf{q}_{int} \quad (3)$$

Light with a frequency ω escaping from the cavity will have the same in-plane component of wavevector (q_x^{ext}), where

$$q_x^{ext} = \frac{\omega}{c} \sin \mathbf{q}_{ext} \quad (4)$$

From the equality $q_x^{int} = q_x^{ext}$ it follows

$$\mathbf{q}_{int} = \arcsin \left\{ \frac{\sin \mathbf{q}_{ext}}{n} \right\} \quad (5)$$

For each cavity mode frequency, the component of the wavevector parallel to the cavity growth direction (q_z) is constant. For each frequency of a given cavity mode, the z component of the wavevector is given by

$$q_z^{cav} = \frac{2p}{l} \cos \mathbf{q}_{int} \quad (6)$$

and is constant and this component is independent of frequency, and is given by $q_z^{cav} = \frac{mP}{L}$. At $\theta_{int} = 0$, the wavelength of the cavity mode is defined as the cut-off wavelength (λ_{cutoff}) – see chapter 3. We can thus relate the wavelength of a light measured outside a cavity to the external viewing angle via

$$l = l_{cutoff} \cos \left(\sin^{-1} \left\{ \frac{\sin \mathbf{q}_{ext}}{n} \right\} \right) \quad (7)$$

If the two mirrors are *closely* separated (i.e. a *microcavity*) it is possible to arrange that there is only one optical mode present that can interact with any semiconductor material placed within the cavity. For example, a cavity fabricated from two mirrors separated by 150 nm, containing a material having $n = 1.5$, the fundamental cavity mode ($m = 1$) will have a wavelength of 450 nm at normal incidence (corresponding to the blue end of the visible spectrum). The next optical mode ($m = 2$) will be positioned at 225 nm (in the deep ultra-violet). The energy separation between these optical modes is 2.75 eV, which is significantly larger than the absorption or emission bandwidth of many organic and inorganic materials.

The structure shown in figure 1 represents an ideal cavity consisting of two completely reflecting surfaces. However such a structure cannot be easily realised in practice (at least at visible wavelengths) as there are no materials available that have unity reflectivity. Microcavities have been fabricated based on two metallic mirrors [Barnes, Cimrova, Bourdon, Burns] (which in the case of silver approximates a perfect reflector), however there are limitations to this approach. To be able to usefully ‘use’ the light emitted from a source inside the cavity, it must escape from the cavity by penetration through one of the cavity mirrors. If the metallic mirrors are thick compared to their optical skin depth, then light cannot escape from the cavity and there is very weak output coupling. If one of the mirrors are thin, then some light can escape from the cavity through the semi-transparent mirror. However the reflectivity of a thin metallic film is significantly lower compared to a bulk film, which results in a microcavity that has a rather low finesse, and only weakly confines photons. In addition, the absorption of light passing through even a thin (20 nm) metallic film is significant, resulting in a microcavity that has quite high losses.

To achieve effective photon confinement within a microcavity, it is more common to utilise dielectric mirrors (distributed Bragg reflectors or DBRs) as the cavity reflectors. Such dielectric reflectors can have a much higher reflectivity than a metallic surface, and have the significant advantage of very low absorption loss. A DBR is a multilayer structure composed of a series of ‘pairs’ of dielectric layers [Hecht]. Each mirror pair is composed of two different dielectric materials, having either a high, or a low refractive index, but with each layer having an optical thickness of $\lambda/4$. DBRs can have a very high optical reflectivity ($> 99\%$) over a range of wavelengths (termed the ‘stop-band’). The high reflectivity of a DBR results from in-phase optical reflections from each of the layers within the dielectric stack. Figure 2 shows the measured reflectivity spectrum from a 12 pair DBR composed of alternate layers of silicon oxide ($n = 1.45$) and silicon nitride ($n = 1.95$), on a polished glass substrate. The mirror has a maximum reflectivity of 99.8% at 525 nm, and a stop-band extending from 475 to 580 nm.

Inorganic semiconductor microcavities are usually composed of two DBRs deposited either side of the active semiconductor layer (which is often comprised of a series of quantum wells). As the semiconductor mirrors are deposited using the same molecular beam epitaxy (MBE) process as the quantum wells, the whole structure can, in principal be grown in a single deposition run. This is usually not possible when creating organic semiconductor microcavities, as the process used to deposit the (usually inorganic) DBR is often very different from that used to deposit the organic semiconductor. For example, the DBR shown in figure 2 was grown by plasma enhanced chemical vapour deposition, which involves reacting two flowing gas streams above a glass substrate heated to 300°C. Such a deposition process is not possible *on top of* an organic semiconductor, as most organic materials suffer significant degradation at temperatures in excess of 250°C. This incompatibility between different processing techniques to some extent restricts the type of structures that can be grown using organic materials. Because of this, most of the organic semiconductor microcavities studied so far have comprised of one DBR and one metallic mirror [Lidzey1, Lidzey2, Lidzey3, Lidzey4, Lidzey5, Fisher, Schouwink]. Metallic thin films can be successfully deposited onto an organic thin film by thermal evaporation, with the organic substrate held at room temperature. This process causes little or no degradation to the optical or electronic properties of the organic material.

Figure 3 shows a schematic figure of an organic semiconductor microcavity based on a metallic mirror and a DBR along with the amplitude of the optical field confined within the cavity as calculated using a transfer matrix reflectivity (TMR) model [Hecht]. This type of structure has been used in all of the experiments described in this chapter. Such microcavities support a $\lambda/2$ optical mode between the two mirrors, whose wavelength can be adjusted by

simply changing the thickness of the organic film. It can be seen that the optical field penetrates a significant distance into DBR dropping off as it approaches the cavity surface in an exponential fashion. Because there is a finite amplitude of the optical field at the DBR surface, light can couple out of the cavity to the outside world. In contrast, light cannot penetrate through the ‘thick’ (>100 nm) silver mirror, and so all experiments on this structure to study the optical properties of the cavity must be performed through the DBR. When fabricating microcavities of this type, it must be remembered that if the reflectivity of the DBR is very much greater than that of the metallic mirror, then the photons within the cavity are more likely to be absorbed within the metallic mirror than escape through a very high reflectivity DBR. Hence with single DBR cavities, there is a practical limitation to the finesse that can be realised. In our work, we have used DBRs consisting of 9 dielectric pairs, having a peak reflectivity of around 98%. Recent reports have however highlighted new techniques used to grow DBR mirrors onto organic semiconductors, and have realised very high finesse microcavities operating in the weak-coupling limit [Anni, Denton]. It will be very interesting to create strongly coupled organic semiconductor microcavities using such procedures.

The linear optical properties of a cavity can be determined by measuring its reflectivity as a function of wavelength. We discuss the practicalities of cavity reflectivity measurement in section 1.4. Figure 4(a) shows a reflectivity spectrum measured for a metal-DBR microcavity containing a single layer of a transparent dielectric polymer (having a thickness of ~ 220 nm and an average refractive index of 1.6). It can be seen that a single sharp ‘dip’ is seen in the reflectivity spectrum at 1.74 eV having a linewidth FWHM (full width a half maximum) of 14 meV. The sharp dip in the reflectivity indicates the presence of an optical mode within the cavity to which photons from the outside world can couple. The dip in reflectivity apparently indicates that such photons do not reappear from the cavity. This is because there are other ‘guided’ optical modes within the cavity that cannot couple to the outside world. If a photon scatters into one of these modes, then it cannot escape from the cavity and can become effectively ‘lost’.

The FWHM of the optical mode ($\Delta\lambda$) is an important parameter in determining the Q-factor of the cavity. The Q-factor is defined as

$$Q = \frac{\lambda}{\Delta\lambda} \quad (8)$$

where λ is the wavelength of the optical mode. The Q-factor relates the energy stored by a (damped) oscillator to the energy dissipated per oscillation cycle, and thus cavities with high Q-factors confine photons for many ‘round-trips’ of the photon. As the linewidth of the cavity mode is homogeneous in nature, it can be used to estimate the lifetime of the confined photons within the cavity via the energy-time representation of the uncertainty principle. For example, a cavity with an optical linewidth of 14 meV will trap photons for around 50 fs. Much higher Q-factors can be realised using cavities based on two DBRs. The highest finesse microcavities to date have been fabricated by Stanley *et al* [Stanley1] and have had linewidths of around 130 μ eV ($Q = 6000$), corresponding to photon lifetimes of approximately 5 ps. As we will show below, the lifetime of the photon within a cavity is an important factor in determining whether strong coupling can occur.

The optical modes supported by microcavities have a strong angular dispersion (see equation 7. This can be readily seen in figure 4(b), which plots the energy of a confined photon mode (determined from the reflectivity spectra), as a function of external viewing angle. The measured photon energy is shown as solid points and the line is a calculation of the photon energy using the analytical expression given in equation 2. The best fit to the data is achieved

using an average refractive index of $n = 1.6$, with photon energy at normal incidence being $E_0 = 1.763$ eV. Figure 4(c) re-plots the data in terms of frequency (ω) versus in plane momentum (q_x). From this data we can deduce an effective photon mass of 10^{-5} of the mass of an electron. We show in the following sections, that the dispersion in the photon energy can be used to tune the energy of the photons with respect to an exciton mode within the cavity and thus explore their mutual coupling.

In our discussion of the optical properties of microcavities, we have so-far only considered ‘empty’ microcavities – i.e. structures that are composed of simple dielectric materials that have no resonant interactions with the cavity photons. We now consider a microcavity containing a semiconductor material, and the interactions that can occur between optically active transitions in the semiconductor and confined cavity photons. There are two distinct interaction regimes that can occur within a microcavity, the weak and the strong coupling regimes. The subject of this chapter is the strong-coupling regime, however for completeness we briefly summarise the salient point of the weak coupling regime.

1.2.2 Weak Coupling

Within the weak coupling regime, the spontaneous emission of a dipole source placed within a cavity can be described via Fermi’s Golden Rule:

$$W_{i \rightarrow f} \propto \langle f | E \cdot \mathbf{m} | i \rangle \mathbf{r} \quad (9)$$

Here the transition rate (W) between initial (i) and final (f) states is proportional to the density of final optical states ρ . The Hamiltonian for the transition is given by $E \cdot \mathbf{m}$ where E is the electric field experienced by an emitter having a transition dipole moment \mathbf{m} . In the weak coupling regime, the microcavity modifies the density of optical states, enhancing them at the cavity mode wavelength, and suppressing them elsewhere. The modification of the frequency dependent density of optical states in the cavity also changes the distribution of vacuum field fluctuations that effectively ‘stimulate’ spontaneous emission: At the cavity mode wavelength, the density of vacuum field fluctuations is enhanced, leading to an increase in the spontaneous emission rate.

If a broad-band emitter is placed into a microcavity, the cavity enhances the emission intensity at the cavity mode wavelength and suppresses it elsewhere, producing a significantly spectrally narrowed source. A number of authors have demonstrated that the intensity of emission can be enhanced at the cavity mode wavelength, in some cavities by up to 60 times [Vredenberg, Lidzey6,]. Fluorescence lifetime emission measurements show however that the *overall* spontaneous emission rate from an excited atom or exciton within a 1-dimensional microcavity is rather small – of the order of 20% at most [Hopmeier1, Jordan]. Such small changes occur because there are a large number of ‘leaky’ modes in a 1-D microcavity, including many guided optical modes in a DBR. These leaky modes limit the overall effect of the cavity on an exciton, with the result being that changes in the spontaneous emission rate are small. A microcavity in the weak coupling regime can thus be thought of a structure which redistributes the emission from a source placed between the mirrors, allowing light to escape from the structure that would otherwise be trapped by total internal reflection.

Such properties are in fact highly desirable as they can be used to enhance the external quantum efficiency of light emitting devices. The strong spectral narrowing that can be achieved is also very useful in display devices, where pure, spectrally narrow emission colours are required to achieve a full colour palette. Figure 5(a) shows a schematic diagram of a light emitting diode

based on a conjugated polymer that has been engineered into a microcavity (a resonant-cavity LED). The structure is based on a DBR, an indium tin-oxide anode (used to inject holes into the conjugated polymer) and a top cathode-mirror, composed of a thin (10 nm) layer of calcium to facilitate the injection of electrons into vacant states in the polymer. A thick layer of aluminium is deposited onto the calcium, to create a reasonably highly reflective cavity mirror.

Figure 5(b) shows the emission from the cavity (open circles) along with the absorption (full circles) and emission (dotted line) from the same conjugated polymer in a non-cavity electroluminescent device. The spectral narrowing of emission from the cavity is very clear, with a strong emission peak visible at 535 nm, having a linewidth of 12 nm. This compares to the electroluminescence emission from a non-cavity LED that has a FWHM of around 90 nm. It can be seen that the emission from the microcavity LED is not completely ‘pure’: there is also weak emission from another feature at 635 nm. This emission comes from a second cavity mode, whose wavelength coincides with the long wavelength emission tail of the polymer. Such bi-modal emission can be easily eliminated by reducing the overall length of the cavity [Fisher, Ho].

1.2.3 Strong Coupling

In a microcavity, the strong-coupling regime is evidenced by an anticrossing between photon and exciton modes, and on resonance the appearance of two equal intensity transitions, separated by the Rabi-splitting energy ($h\Omega_{Rabi}/2p$). Such a splitting can only be realised when the interaction strength (expressed as an angular frequency Ω_{Rabi}) between a photon and an exciton is greater than (i) the inverse cavity photon lifetime and (ii) the inverse exciton dephasing time. Condition (i) dictates that the photon is confined in the cavity for a time that is longer than the period of the Rabi oscillations ($2p/\Omega_{Rabi}$). Condition (ii) ensures that an ensemble of excitons retain their mutual coherence in their wavefunctions for a time which is also longer than the Rabi oscillation period. If either of these conditions is not met, then a coherent superposition of states cannot be formed because either the photon leaks from the cavity, or the exciton undergoes dephasing before one period of oscillation between the exciton and photon modes can occur. In this case, the system is in the weak coupling limit and the exciton decays by spontaneous emission. It is common to express such inequalities in terms of the homogeneous energy linewidths of both the exciton (Γ_{ex}) and the photon modes (Γ_p); thus

$$\Gamma_{ex} < h\Omega_{Rabi}/2p \quad (10)$$

$$\Gamma_p < h\Omega_{Rabi}/2p \quad (11)$$

It is also important to consider the *inhomogeneous* linewidth when deciding whether strong coupling can be achieved. To be able to resolve a splitting between a photon and an inhomogeneously broadened semiconductor transition, the inhomogeneous linewidth also needs to be narrower than the Rabi-splitting energy. To a first approximation, the Rabi-splitting energy can be expressed using

$$\frac{h}{2p} \Omega_{rabi} \propto \sqrt{\frac{f}{n_c^2 L_{tot}}} \quad (12)$$

where f is the oscillator strength of the semiconductor excitons per unit area, n_c is the average refractive index of the semiconductor and L_{tot} is the *physical* path length of the cavity. The oscillator strength f per unit area of a thin film is given by

$$f \propto \alpha L \quad (13)$$

where L is the film thickness, and α is the optical attenuation coefficient (per unit path length) at the peak of the absorption. If the inhomogeneous linewidth of the semiconductor material is very broad, then the oscillator strength of the transition is effectively spread over frequency space, and thus the peak value of f that is achievable is relatively small. A reduced value of f results in a reduced Rabi-splitting, with a possible consequence being that the Rabi-splitting becomes smaller than the inhomogeneous linewidth of the excitons. In this case the broad inhomogeneous linewidth of the excitons (which encompasses a large distribution of narrower homogeneous states), results in a distribution of reduced coupling strengths, effectively masking the anticrossing behaviour. The eventual consequence of using states with very broad inhomogeneous linewidths is that the system operates in the weak-coupling regime.

The operation of a material system in the weak coupling regime can be seen in figure 5(b). Here the organic semiconductor used has rather broad and featureless transitions, which are characterised by transition linewidths of the order of 500 meV. Such a material system would not be anticipated to undergo strong-coupling, as it effectively constitutes a continuum of states. In addition, in this structure, the cavity mode has been deliberately positioned at a wavelength that coincides with a region of high electroluminescence emission intensity from the conjugated polymer. Because of the large Stokes shift in this material system, there is a very low residual absorption (and thus no transition having significant oscillator strength) at the cavity mode wavelength, again indicating that the system operates in the weak coupling limit.

1.3 Organic Semiconductors for Strong Optical Coupling

1.3.1 Background

Before we discuss strong coupling of organic semiconductors, it is useful to briefly describe the magnitude of the Rabi-splitting observed in microcavities containing inorganic (III-V) QW excitons. The inhomogeneous linewidth of a QW exciton (which is often broadened by fluctuations in the alloy composition of the inorganic crystal, and also by roughness in the thickness of the quantum well) is typically around 1 meV. By utilising highly reflective semiconductor DBRs, it is relatively straightforward to create microcavities supporting confined photon states having linewidths of 1 meV. In microcavities based on III-V semiconductor quantum wells (utilising GaAs/InGaAs), Rabi splittings of around 5 meV have been observed (at 20K) [ref]. Therefore the homogeneous and inhomogeneous linewidths of both the photon and exciton are smaller than the Rabi splitting, satisfying the inequalities given in equations 5 and 6.

1.3.2 Molecular Dyes

As we have discussed in section 1.2.3, to achieve strong optical coupling, it is necessary to use semiconductor materials whose absorption linewidths are narrow compared to the Rabi-splitting energy. The materials we have used to achieve strong-coupling have had inhomogeneous absorption linewidths between 40 and 90 meV. This linewidth is well over an order of magnitude larger than the Rabi-splitting observed in III-V QW microcavities. However this relatively broad linewidth has not precluded organic semiconductors from reaching the strong-coupling regime; this is because the oscillator strength of a thin film of an organic semiconductor can be at least

two orders of magnitude larger than that of a series of inorganic QWs. It can be seen from equation 7, that the Rabi-splitting energy is proportional to \sqrt{f} , and thus the Rabi-splittings that we observe can be significantly larger than the relatively broad linewidth of the organic semiconductors that we have used in our microcavities.

In our microcavities, we have used organic materials that we have used have the distinct advantage that they are relatively easy to fabricate into high-quality, defect-free, thin films suitable for inclusion into a microcavity. In our first observation of strong coupling in a microcavity [Lidzey1], we used a porphyrin dye having a single narrow optical absorption. The dye used (tetra-(2,6-*tert*-butyl)phenol-porphyrin zinc) which we term 4TBPPZn is one example of a large family of porphyrin macrocycles whose photophysical and photochemical properties have been extensively studied [Porphyrin]. The chemical structure, absorption spectrum and electronic energy-level scheme of the 4TBPPZn molecule are shown in figure 6(a). This molecule has an intense, narrow (90 ± 5 meV at room temperature) transition in the form of the so called "Soret band" absorption at 2.88 eV. The relatively narrow linewidth of the optical absorption comes from the high structural rigidity of the porphyrin molecule. The Q-band absorbance is seen as a weak double peak structure between 2.0 and 2.26 eV.

To utilise the 4TBPPZn molecular dye in a microcavity, it was dissolved into a solution of toluene containing the polymer polystyrene. The solution was then spin-coated onto a quartz substrate. On spin-coating, the toluene solution rapidly evaporates, leaving the 4TBPPZn molecules suspended in a solid polystyrene matrix. This deposition method allows the creation of films having areas of up to several cm^2 with a thickness anywhere between 30 nm and $1\mu\text{m}$. The point-to-point fluctuations in the film thickness over an area of around 1 cm^2 can be relatively small (of the order of 5 - 10 nm). By careful calibration of the viscosity of the solution and spin-speed, the thickness of the film deposited can be controlled with a precision of about 10 nm. The attainment of very smooth organic films is critical for the fabrication of high-quality microcavities. Any surface roughness or scattering within the film will lead to a significant broadening of the cavity optical mode.

The absorption spectrum of the polystyrene film containing the 4TBPPZ molecules is shown in figure 6(a). The polystyrene matrix has an average refractive index of approximately 1.5, and has a very high degree of optical transparency over the whole of this visible spectrum. The use of a matrix polymer to suspend the active molecules is an important feature of our approach. The matrix physically separates the molecules from one another by suspending them in a 'solid solution'. It is of course possible to create a 'pure' thin film of 4TBPPZn molecules directly via spin-coating or by thermal evaporation without the use of a matrix film, however the strong intermolecular interactions that occur in such molecular films tend to significantly broaden the Soret-band absorption and reduce the possibility of achieving strong coupling. Figure 6(b) shows the absorption of a thin film of 'pure' 4TBPPZn molecules that have been deposited by spin-coating. It can be seen that the Soret-band absorption has now broadened, having a linewidth of approximately 220 meV. There is also an absorption background visible in the spectrum, whose origin comes from scattering. This scattering results from micro-crystallinity within the film, again resulting from the strong intermolecular interactions that occur when a matrix polymer is not used. Such scattering would significantly reduce the finesse of the microcavity, and make strong-coupling much more difficult to achieve.

1.3.3 J-Aggregates and other Self-Assembled Molecular Systems

A second type of organic semiconductor system that we have used for strong coupling is based on J-aggregates of cyanine dyes, which are a class of material that has found diverse uses in photography [Sturmer] and as laser dyes [Bos]. Cyanine dyes carry a net charge, which drives

a self-assembly of the molecules in a polar solution to form 1-dimensional aggregates termed J-aggregates [Mobius, Potma, Kobayashi]. Intermolecular interactions in J-aggregates is responsible for the appearance of an excitonic band. Due to the ‘head to tail’ packing of the molecules in the aggregate the lowest energy state in the band has zero wavevector. To a first approximation we can say that optical transitions are only permitted to the lowest energy point in the band. For this reason and due to phenomena resulting from motional narrowing [Knapp], J-aggregate absorption spectra are often characterised by a single, relatively narrow and intense optical transition, significantly red-shifted from the absorption of the un-aggregated monomer. Following optical excitation, the primary fundamental excitations that are created in the aggregate are singlet excitons. Such excitons have relatively large binding energies, which allow them to be created and studied at room temperature. In J-aggregates, the excitons are highly mobile and can be viewed as being delocalised over a relatively large number of molecular units.

To process cyanine dyes into microcavities, the J-aggregates were suspended in a polymer matrix. Cyanine dyes are usually soluble in polar solvents such as water and methanol, and thus we have used the matrix material poly(vinyl alcohol) [PVA] which is also soluble in aqueous solvents. Strong-coupling has been achieved with two different J-aggregate forming dyes (whose chemical structures are shown in the insets in figures 7(a) and 7(b) [refs]). To fabricate a thin film of J-aggregates, the cyanine dye is dissolved at a concentration of ~ 1 mg / ml into a 50/50 water-methanol mix containing the PVA polymer. Thin films of the composite organic film were formed by spin-coating. During the spin-coating process, the water and methanol evaporate, which rapidly raises the concentration of the cyanine dye. This drives an association of the molecules to form the J-aggregates. Figure 7(a) and (a) shows the optical absorption and photoluminescence of two different PVA / J-aggregate thin films. The J-aggregates shown in figure 7(a) have an absorption peaking at 1.84 eV, with a linewidth of 40 meV. The absorption is slightly asymmetric, having a weak tail that extends to higher energies. The PL is the mirror image of the absorption, and is Stokes shifted down in energy by 5 meV.

This solution based deposition method is critical for the formation of the J-aggregates. If a thin film of the cyanine dye is deposited by a non-aqueous method (for example by thermal evaporation), the molecules are unable to associate with one another and the formation of the 1-dimensional aggregates is blocked. This is highlighted by the absorption spectra shown in figure 8. For ease of comparison, we plot the normalised absorption of an amorphous cyanine dye film formed by vapour deposition along with the same material in a PVA matrix which has self assembled in solution to form J-aggregates. However, the peak absorption of J-aggregated film would be much more intense than that of an amorphous film containing the same number of monomers per unit volume. To a good first approximation, the oscillator strength of each of the monomers is concentrated into the J-aggregate transition band. It can be seen that the J-aggregate absorption is located at the extreme low-energy end of the monomer absorption. Whilst the aggregated molecules are a good candidate for strong-coupling, the amorphous material clearly is not. There is thus a subtle difference in the use of J-aggregates for strong coupling as apposed to the use of highly rigid molecular dyes as exemplified by the material system shown in figure 2: Here, we do not rely on the structural rigidity of the molecule to create a narrow optical transition. Instead the narrow transition arises because of the natural tendency of the molecules to self organise into molecular superstructures which have delocalised and narrow optical transitions, determined by the structure of the molecular packing.

One consequence of the self-assembly of the cyanine dye molecules during the spin-coating process is a degree of inhomogeneity in their spatial distribution. Figure 9(a) shows the transmission signal recorded using a near field optical microscope (SNOM) from a thin film (30 nm) of the J-aggregates in a PVA matrix whose emission and absorption spectra are shown in figure 7(a). The image was generated by scanning a SNOM probe (having a 100 nm aperture)

over the surface of the PVA-J-aggregate film, and monitoring the relative transmission of a HeNe laser (632.8 nm) through the film. As the wavelength of the laser is within the high energy absorption tail of the J-aggregates, it is possible to assign variations in the intensity of the transmitted signal to the distribution of the aggregates. Figure 9(b) shows the physical topography of the thin film recorded simultaneously using a shear-force technique. It can be seen from figure 9(b) that the surface of the film is flat to within 15 nm. The transmission signal however shows strong spatial variation, and a number of regions of strong absorption are detected, having characteristic length-scales of around 250 nm. It is therefore clear that there is inhomogeneity in the distribution of the aggregates and the local oscillator strength over the surface of the film

We do not anticipate that these features correspond to single aggregates. It is more likely that within each of these structures there is a sub-structure which is unresolved by our microscope system. We can in fact estimate the number of molecules within each aggregate on the basis of the reduction in the linewidth of the J-aggregate absorption compared to the monomer absorption. It has been shown [Knapp], that the inhomogeneous linewidth of an aggregate composed of N molecules scales with $N^{1/2}$. For the material system shown in figure 8, the linewidth of the J-aggregate is approximately 10 times smaller than that of the monomer, implying that each aggregate is comprised of about 100 coupled-molecules. We estimate the length of a single molecule to be 2 nm, and allowing for some overlap between the neighbouring molecules in the aggregate, we calculate the average length of a J-aggregate to approximately 100 to 150 nm. In the PVA matrix film, we estimate that there are approximately 2×10^{17} aggregates per cubic centimetre, implying an average inter-aggregate separation of 20 nm. From this simple estimation, it can be seen that each feature in the transmission image shown in figure 9(a) is therefore likely to comprise of many individual uncorrelated aggregates.

Strong-coupling effects have also been observed using perovskites. Perovskites are self assembled systems, that form alternate nano-structured organic and inorganic layers [Era]. Such materials can be thought of as analogous to inorganic quantum well heterostructures: in a perovskite, the organic component of the complex $[\text{C}_6\text{H}_5\text{C}_2\text{H}_4\text{NH}_3]$ acts as the barrier for the inorganic well material [a PbI_4 salt]. The excitons are localised within the inorganic well and have absorption linewidths of around 100 meV. Both synthetic opals [Tsutsui] and distributed feedback gratings (DFBs) [Fujita] have been infiltrated with perovskites, and strong-coupling behaviour has been evidenced.

1.4 Optical Measurement Techniques

One of the simplest techniques used to characterise microcavities is the measurement of reflectivity as a function of angle. This allows the direct determination of the energy and dispersion of the optically accessible states within the cavity. ‘Photon-like’ cavity modes can be readily identified by a sharp dip in the cavity reflectivity spectra. Such photonic modes in microcavities have a strong angular dispersion, with their wavelength at external viewing angle θ given by equation 2.

The angular dependent reflectivity spectra of our microcavities can be measured using the apparatus shown schematically in figure 10. The microcavity (MC) is mounted on a central stage, to which are fixed 3 optical rails, each having free independent rotation around the central axis. Light from a tungsten projector lamp is imaged onto a $500\mu\text{m}$ spot on the microcavity surface via lens L1. The specular reflection from the cavity is collected by a lens L2 and imaged into a fibre bundle (FB) which is also mounted on the optical rail. The fibre-bundle is then used to deliver the reflected light to a cooled CCD spectrograph. Using this equipment, the white light reflectivity

of the microcavity can be measured at angles from 12° to 85° . A polariser (P) placed in front of lens L2 allows either TE or TM polarisations of reflected light to be detected. By comparing the reflectivity of a microcavity to that of an aluminium mirror (which is assumed to reflect light with approximately equal efficiency over the whole visible range) the absolute reflectivity of the cavity can be determined.

Using the system shown in figure 10, we are also able to generate and detect photoluminescence emission from the microcavity as a function of angle. Light from a laser is focussed into a fibre bundle, one end of which is mounted on an optical rail. The laser light delivered by the fibre is then focussed by lens L3 onto a $500\ \mu\text{m}$ spot on the cavity surface. This system allows the photoluminescence and reflectivity to be measured from exactly the same spot on the cavity surface. This apparatus is designed to allow measurements to be made at room temperature and in air. For most purposes this is sufficient, as the organic materials that we use have reasonable photostability. However for some measurements (particularly those involving the use of lasers with high excitation density) it is preferable to mount the microcavity in a cryostat at low temperature. A second similar system measurement is available having a wide angular access cryostat mounted on a rotation stage.

1.5 Dispersion of Cavity Polaritons

1.5.1 Reflectivity Measurements of Strongly-Coupled Cavities

As discussed above, the energy of the cavity photon mode varies strongly as a function of angle, shifting to higher energies at off axis viewing angles. This effect can be conveniently used to tune of the interaction between the exciton and photon modes: the exciton transition energy is to a very good approximation angle independent and hence changing the angle of incidence allows one to adjust the relative separation of the photon with respect to the exciton. We illustrate this point with measurements on microcavities containing a layer of polystyrene doped with 4TBPPZn molecules (whose structure is shown in figure 6(a)). Microcavities were fabricated such that the cavity mode was at a lower energy than the exciton at normal incidence by some 100 to 150 meV and became resonant with it at approximately 35 to 40° . The room temperature reflectivity of a microcavity measured at normal incidence to the cavity axis is shown in fig. 11, curve A. The cavity photon mode is visible as a sharp dip in the reflectivity at 2.68 eV. The 4TBPPZn exciton absorption lies at 2.88 eV (marked by the dashed vertical line). The exciton can only just be detected at normal incidence in the reflectivity spectrum as there is very little coupling between the photon and exciton modes as they are relatively far apart in energy. As the cavity mode is tuned closer to the exciton energy, strong-coupling is observed (curve B). The two modes of the system can now no longer be described as ‘pure photon’ or ‘pure exciton’; rather each mode must be described as a linear superposition of photon and exciton. The exciton-like mode thus becomes increasingly visible in reflectivity, as it contains an increasing large cavity-photon like character. Such mixed modes are termed cavity polaritons. On resonance (curve C) the expected pair of equal intensity Rabi-split transitions are seen both containing equal admixtures of a photon and an exciton. For larger angles, beyond resonance (curve D) the coupling reduces, again in line with expectation. Such spectral features are entirely consistent with other measurements made on strongly-coupled inorganic-semiconductor microcavities [refs].

The energies of the two transitions are plotted in fig. 12 as a function of the angle of incidence. The horizontal dashed line at 2.88 eV is the 4TBPPZn exciton energy in the polystyrene blend film. This energy is angle independent and hence defines the resonance energy

for the coupled exciton-photon system. The cavity photon and 4TBPPZn exciton modes exhibit a very clear anti-crossing behaviour and the Rabi-splitting energy, of 110 meV between the two transitions at the 40° resonance angle is *exceptionally large*.

1.5.2 Macroscopic and Microscopic Analysis of Dispersion

The structure that we consider is very disordered. However the distance between the dye molecules in the microcavity is approximately of 2 to 3 nm, and is thus much smaller than the wavelength of the optical mode. This means that we can use an equation of macroscopic electrodynamics, with some dielectric constant to describe the optical properties of the cavity. We can write following Maxwell's equations for a light wave in a three dimensional isotropic medium

$$\frac{k^2 c^2}{\omega^2} = \mathbf{e}(\omega) \quad (14)$$

where ω and k are the frequency and wavevector of a light wave. This equation determines the dispersion relation of the frequency to the wavevector. However let us firstly consider a microcavity having a material that has an optical resonance which is very far from the cavity cut-off frequency. In this case, the dielectric constant ϵ_o can be considered a constant, thus

$$\frac{k^2 c^2}{\omega^2} = \mathbf{e}_o \quad (15)$$

For the m^{th} cavity mode k_z is fixed, and in this case

$$k^2 = k_x^2 + \left(\frac{m\pi}{L} \right)^2; m = 1, 2, \dots \quad (16)$$

where k_x is the in-plane component of the total wavevector. From equations 14 and 15, it is easy to show that for small k_x , the dependence of the frequency of the cavity mode on its in-plane wavevector is given by

$$\omega^{cav}(k_x) = \omega_{cutoff} + \frac{h k_x^2}{4 \mu m} \quad (17)$$

where ω_{cutoff} is given by

$$\omega_{cutoff} = \frac{c}{\sqrt{\epsilon_o}} \left(\frac{m\pi}{L} \right) \quad (18)$$

and μ is the effective mass given by

$$\mu = \frac{h \omega_{cutoff} \epsilon_o}{2 \pi c^2} \quad (19)$$

In organic materials ϵ_o is of the order of 3, and as the cutoff energy in our cavity is given by $\hbar\omega_{\text{cutoff}}/2\pi \sim 2$ eV, we calculate the cavity photon effective mass to be of 10^{-5} of a free electron.

If a material is placed within the cavity, having an (excitonic) resonance given by

$$\mathbf{e}(\mathbf{w}) = \mathbf{e}_o + \frac{2E_o f}{E_o^2 - E^2 - 2ig(E)E} \quad (20)$$

where f is some constant proportional to the oscillator strength, E_o is the resonance energy of the exciton, and γ is the homogeneous broadening. In the case where $E \approx E_o$ the resonance term can be simplified and it can be shown that

$$\mathbf{e}(\mathbf{w}) = \mathbf{e}_o + \frac{f}{E_o - E} \quad (21)$$

where we neglect the term accounting for homogeneous broadening. Substituting equation 21 into equation 14, and using equations 16 and 17, it can be shown that the dispersion of the cavity polaritons is given by

$$[E_c(k_x) - E](E_o - E) = V^2 \quad (22)$$

where the energy of an optical mode in an bare cavity is given by

$$E_c(k_x) = \left(\frac{\hbar}{2\mathbf{p}} \right) \mathbf{w}^{\text{cav}}(k_x) \quad (23)$$

and V is given by

$$V = \sqrt{\frac{fE_o}{2\epsilon_o}} \quad (24)$$

and is half the Rabi-splitting energy. For the derivation of the above equations, we used a phenomenological Maxwell equation. The results of this derivation, summarised by equation 22 are identical to the results of microscopic theory, which are usually used in the analysis of inorganic semiconductor microcavities. Our derivation presents a straightforward approach to determine the main features of the Rabi-splitting if the dielectric constant of the organic semiconductor within the cavity is known. At the same time, it can be generalised to take account of both homogeneous and inhomogeneous broadening.

However we now proceed in our analysis of the strongly coupled microcavity using a microscopic theory. This method is widely used in the description of inorganic semiconductor microcavities. The cavity is described as a compound oscillator consisting of the exciton and photon modes. The compound oscillator is described with the matrix equation

$$\begin{pmatrix} E^{\text{cav}}(k_x) - E & V \\ V & E_o - E \end{pmatrix} \begin{pmatrix} \mathbf{a} \\ \mathbf{b} \end{pmatrix} = 0 \quad (25)$$

E_o and V are assumed to be constant at all angles. In equation 25, α and β are the coefficients of the bare photon and exciton respectively, which describe the weighting of each of the states in the coupled modes. The matrix can be diagonalized to obtain the eigenvalues of the system (E) which represent the energy of the polariton branches, and the coefficients α and β . Equation 25 can be solved analytically, and for the case of the photon resonant with the exciton ($E^{\text{cav}} = E_o = \epsilon$), it is straightforward to show that the two polariton branches have energies given by

$$E_{\pm} = e \pm V \quad (26)$$

where $2V = (\hbar/2\pi)\Omega_{\text{Rabi}}$. To compare with the experimental data, the photon energy dispersion $E_{\text{ph}}(\theta)$ is calculated via a transfer matrix model in which the only free variables are the photon energy at 0° and the average (non-dispersive) refractive index of the cavity. The solid line displayed in figure 12 is the energy of the two polariton branches calculated using equation 25. As it can be seen, the agreement between the data obtained from experiment and the coupled oscillator model is excellent. Figure 13 plots the values of α^2 and β^2 for the upper and lower branches. At small angles the upper branch only contains a small component of the cavity photon, and is thus weak in reflectivity (see curve A, figure 11). As the viewing angles increases, the upper-branch photon component grows, and thus it becomes more visible in reflectivity (curve B). At resonance (40°), the cavity photon is contained equally in both branches, and thus they are detected with equal intensity in reflectivity (curve C). Beyond resonance, the cavity photon is largely contained within the upper polariton branch, which thus becomes increasingly dominant in the reflectivity spectrum (curve D).

The excitons within the cavity can be viewed as an ensemble being driven by the confined optical field. The coupling between the exciton mode and the photon mode necessarily implies a mutual *coherence* between the excitons in the microcavity. The polarisability of the organic layer per unit area is therefore dependent on the sum of the oscillator strength of all the molecules within the cavity. By adjusting the concentration of the 4TBPPZn dye in the blend film it is possible to control oscillators strength of the organic layer, and thus adjust the energetic splitting between the two branches. This is summarised by equations 12,13 and 24 which show that the Rabi-splitting varies as the square root of the absorbance. Figure 14 shows the Rabi-splitting energy of a series of microcavities plotted as a function of $(\alpha L)^{1/2}$: The observed proportionality is in good agreement with expectation. The largest room temperature Rabi-splitting that we have measured, is 160 meV; more than 30 times the typical splittings observed for III-V quantum well microcavities, which are of the order of 5 meV [ref]. In the appendix, we show that the oscillator strength of the 4TBPPZn film that gave a Rabi-splitting of 160 meV is approximately 100 times larger than that of a series of three III-V QWs. This increase in oscillator strength enhances the Rabi-splitting by a factor of 10. Two important additional effects also contribute to the enhanced Rabi splitting observed in the organic semiconductor microcavity compare to its inorganic analogue. These are the low refractive index of the organic layer and the use of a metallic reflector. We show in the appendix that these factors increase the local optical field experienced by the semiconductor, and enhance the Rabi-splitting (compared to a III-V QW microcavity) by a factor of approximately 3.3 times.

1.6 Cavity Emission Following Non-Resonant Laser Excitation

In the previous section, it was demonstrated that organic semiconductor microcavities can show giant Rabi-splittings due to the very large oscillator strength of organic excitons. In this section we turn our attention to the photon emission from an organic semiconductor microcavity

following non-resonant optical excitation. In our work [Lidzey2, Lidzey8], we have used J-aggregates of a cyanine dye instead of the 4TBPPZn material discussed in the previous section. This change in molecular system does not result in any particularly different linear optical properties of the cavity, apart from a change in the resonance energy of the system. However as shown in figure 7, the J-aggregates that we have studied can emit strong fluorescence following optical excitation. This fluorescence emission is a convenient probe by which to study the effect of strong-coupling on the excitons within the cavity.

1.6.1 Experimental Observations

The apparatus shown in figure 10 was used to excite and then detect emission from the cavity following non-resonant excitation. In a non-resonant excitation experiment, photons having an energy greater than that of the polariton branches are shone into the cavity. The photons directly excite excitons in the cavity, which relax in energy and populate the ‘exciton-reservoir’. The exciton reservoir describes the population of excitons within the microcavity, that have either an energy or in-plane momentum that is greater than that of the polariton modes. Such excitons cannot directly couple to a cavity photon. Instead, the population of the polariton states can only occur once the excitons have lost an appropriate amount of energy or momentum through phonon emission. A number of authors have studied the emission from cavity polaritons following non-resonant excitation [Houdre2, Wainstain2, Wainstain3, Wainstain4, Sasha2, Stanley3]. We will show that our results are in accord with the observations made in microcavities containing inorganic QWs, giving us further confidence of the strong-coupling picture that we use to describe our microcavities.

To generate *cw* photoluminescence emission from the cavity, light from a red HeNe laser (having an energy of 1.96 eV) was focussed into the cavity through lens L3 (see figure 10) at normal incidence (having a power density at the cavity surface of 50 kW m^{-2}). It can be seen from figure 7(a), that the energy of the excitation photons lie within the high energy tail of the J-aggregates. The excitation is non-resonant, as the laser photons have an energy 110 meV greater than the peak absorption energy of the excitons (1.84 eV). The photon emission from the cavity was collected using lens L2, and was imaged into a fibre-bundle connected to a CCD spectrograph.

Figure 15(a) shows the relative reflectivity of the cavity measured at a series of increasing viewing angles. At 20° , two modes are visible: a sharp dip at 1.72 eV (a photon-like mode), and a second weaker dip at 1.85 eV (an exciton-like mode). Resonance between the exciton and photon occurs at 45° degrees, where two equal intensity modes are visible, split around the peak absorption energy of the excitons (which is marked with a vertical dashed line). At viewing angles greater than 45° , the higher-energy mode moves to higher energies. This behaviour is consistent with absorption and reflectivity spectra measured from microcavities containing 4TBPPZn described in the previous section.

Figure 15(b) shows the photon-emission from the cavity, recorded at a number of different viewing angles. The emission from the lower-branch is more intense than the upper-branch at all angles. Very similar behaviour has been reported from microcavities containing III-V semiconductor QWs [Stanley3]. The upper polariton branch (located at 1.85 eV at 20°), decreases in intensity as a function of increasing viewing angle. At angles of 35° and above, two features are detected in emission in addition to that from the lower-branch. This point is further illustrated in figure 16, which plots the emission measured at 35° . The spectrum can be well described using 3 Lorentzian functions as shown. The higher and lower energy features can be

positively identified as emission from the upper and lower branches, as their energy coincides with the energy of the features recorded in reflectivity (see fig 15(a)). The energy of the central feature appears to coincide with the peak emission energy of the J-aggregates (see figure 7(a)). It therefore appears that some of the J-aggregates emission ‘escapes’ from the cavity without coupling to a cavity-polariton mode. At present, the reason for such ‘uncoupled’ emission is not fully understood, however similar observations have been made in inorganic semiconductor microcavities, and have been attributed to emission from localised states [Muller] and inhomogeneous broadening [Houdre].

Figure 17(a) shows a plot of the peak photon-emission energy from the two branches as a function of angle (solid points). The open circles mark the energy of the feature that we identify as uncoupled exciton emission. It can be seen, that the polariton branches undergo anticrossing around an energy coinciding with the peak of the J-aggregate absorption (which is marked by a dashed line). The energy of the direct exciton emission remains approximately constant as a function of angle as expected. A Rabi-splitting of 80 meV is detected between the polariton branches at an angle of 42.5°. Figure 17(b) shows a plot of the photoluminescence emission intensity from a control film of J-aggregates. It can be seen that the J-aggregate emission spectrum is approximately symmetrical with respect to the energy at which anticrossing occurs (1.84 eV). This symmetry is not however reflected in the emission intensity from the two polariton branches which are strongly asymmetric (see figure 15(b)). At resonance, the emission intensity from lower branch is 14 times larger than that from the upper branch.

1.6.2 A model for non-resonant excitation and emission

We now describe a model that we have used [Lidzey8] to describe the angular dependent emission intensity from the microcavity. The model considers the scattering of excitons from the exciton reservoir into the upper and lower polariton branches, followed by their radiative decay. Our model provides a good fit to the experimental data, provided that a term is included which allows a transfer of the polariton population to occur from the upper to the lower branch. The model is summarised schematically in figure 18.

We first calculate the weight of the exciton and photon modes in the polariton branches as a function of angle using equation 10. The best-fit theoretical dispersion for the energy of the polariton branches is shown as a solid line in figure 16(a) and is in good agreement with the experimental data. We also introduce the labels u and L to denote the upper and lower branches respectively. Unless stated, all terms are expressed as function of viewing angle (θ).

We assume that the polariton branches are populated by direct scattering of excitons from the reservoir. Furthermore we make the common assumption [scattering] that the scattering rate of excitons from the reservoir to a polariton state is directly proportional to the relative exciton fraction ($\mathbf{b}_{u,L}$) of the polariton state. The population rate of the branches $P_q^{u,L}(\omega)$ is thus given by

$$P_q^{u,L}(\omega) = \Phi U_{u,L}(\omega) \mathbf{b}_{u,L}^2 \quad (27)$$

where $U_{u,L}(\omega)$ is the relative number of uncoupled excitons in the reservoir having the appropriate energy to scatter into the state, and Φ is a scaling constant, dependent on the intensity of the excitation laser. We assume that the distribution of $U(\omega)$ is the same as the photoluminescence emission spectra – i.e. the spectra this provides a measure of the distribution of energetically relaxed excitonic states within the J-aggregate. We assume that exciton scattering occurs from the reservoir to a polariton state, and there is no return path back to the reservoir.

This is because the radiative rate of polaritons from the cavity is likely to be much faster than the relatively slow scattering process.

We introduce a population transfer term *between* the branches. We propose that population-transfer occurs by the emission of energy in the form of vibrational quanta. Such a transfer process will occur when $E_u - E_L = \hbar\nu_{\text{phonon}}$. Figure 19 shows a resonance Raman spectrum recorded for the J-aggregate material used in this experiment. It can be seen that there is a strong Raman-active mode having an energy of 74 meV. In this particular cavity, the Rabi-splitting between the cavity branches on resonance is 80 meV; an energy almost resonant with that of the Raman mode. The slight difference between these two energies is smaller than the linewidth of each of the polariton branches, which have a FWHM of approximately 30 meV. This broadening also means that phonon-mediated inter-branch transitions are permitted over most of the detuning range studied in this experiment.

In our model, we assume that polariton transitions between the branches occur between initial and final states having the same in-plane momentum. This adiabatic approximation regards the high frequency optical phonons as a slow subsystem being strongly localised and having an effective mass at least 100 times larger than that of the exciton [Agranovich3]. We neglect momentum transfer to the optical phonon, with only energy in the $u \rightarrow L$ transition being conserved. The interaction with molecular vibrations is maximised when the polaritons in both branches are exciton like, and thus the transition rate between the branches $\rho(\theta)$ is given by

$$\mathbf{r}(\mathbf{q}) = K_{u \rightarrow L} \mathbf{b}_u^2 \mathbf{b}_L^2 \quad (28)$$

where $K_{u \rightarrow L}$ is a rate-constant, assumed to be constant at all angles and branch separations. As the Rabi-splitting between the branches is much larger than kT , we assume that population transfer occurs from the upper to the lower branch only, and that there are no back-transfer processes.

We now consider the radiative decay of the polariton states. The radiative decay time of a polariton state $\tau_{u,L}(\theta)$ is given by

$$\mathbf{t}_{u,L}(\mathbf{q}) = \frac{\mathbf{t}_{cav}}{\mathbf{a}_{u,L}^2(\mathbf{q})} \quad (29)$$

where τ_{cav} is the escape time of an uncoupled photon from the cavity.

The relative populations of the upper $[N_u(\theta)]$ and lower $[N_L(\theta)]$ polariton branches can be described with the two rate equations:

$$\dot{N}_L(\mathbf{q}) = -\frac{N_L(\mathbf{q})}{\mathbf{t}_L(\mathbf{q})} + \mathbf{r}(\mathbf{q})N_u(\mathbf{q}) + P_q^L(\mathbf{w}) \quad (30)$$

$$\dot{N}_u(\mathbf{q}) = -\frac{N_u(\mathbf{q})}{\mathbf{t}_u(\mathbf{q})} - \mathbf{r}(\mathbf{q})N_u(\mathbf{q}) + P_q^u(\mathbf{w}) \quad (31)$$

Here, the first term on the right-hand-side describes the radiative depopulation of the branches. The second term represents the population transfer from the upper to the lower branch, and the last term describes the filling of the upper and lower branches from the exciton reservoir. As our experiments measure the cw emission from microcavity, we set $\dot{N}_u = \dot{N}_L = 0$. The emission intensity from the cavity $[I_{u,L}]$ can be expressed in terms of the relative polariton population and its radiative decay time:

$$I_{u,L} = \frac{N_{u,L}}{\mathbf{t}_{u,L}} \quad (32)$$

It can be shown that

$$I_u(\mathbf{q}) = \frac{\Phi U_u(\mathbf{w}) \mathbf{b}_u^2}{1 + \mathbf{r}(\mathbf{q}) \mathbf{t}_{cav} \mathbf{a}_u^{-2}} \quad (33)$$

$$I_L(\mathbf{q}) = \Phi \left[\frac{U_L \mathbf{b}_u^2}{1 + \mathbf{a}_u^2 \mathbf{r}^{-1}(\mathbf{q}) \mathbf{t}_{cav}^{-1}} + U_L(\mathbf{w}) \mathbf{b}_L^2 \right] \quad (34)$$

Our model only includes population transfer between branches, it does not account for any redistribution *along* each polariton branch by intra-branch scattering. Such intra-branch scattering processes have been shown to only become significant at laser fluxes much larger than that used in this experiment (i.e. $> 50 \text{ kW m}^{-2}$) [Sasha2].

Figure 20 shows a fit of equations 18 and 19 to the measured angular dependent intensity from the upper and lower branches. The only free variables used in the fit was the product of $K_{u \rightarrow L} \cdot \tau_{cav}$ (which represents the relative competition between the inter-branch transition rate and radiative decay) and Φ . We determine a best fit using a value of $K_{u \rightarrow L} \cdot \tau_{cav} = 4.5$. The measured data points are shown as solid circles, and the best fit to the data is shown as full lines. The agreement between the data and the fit is quite reasonable and in particular it replicates the strong asymmetry in emission intensity observed between the upper and lower branches. Using a bare cavity linewidth of 20 meV, we calculate a photon escape-time from the cavity of $\tau_{cav} \sim 35 \text{ fs}$. The transition rate between the branches [$\rho(\theta)$] is given by equation 13. This term takes its maximum value at resonance, where both $\mathbf{b}_u^2 = \mathbf{b}_L^2 = 0.5$, with their product being equal to 0.25. In this microcavity, resonance between the photon and exciton occurs at 42.5° , thus the maximum transition rate from the upper to the lower branch is given by $\mathbf{r}(42.5^\circ) = 0.25 K_{u \rightarrow L}$. From the best fit, we determine an inter-branch transfer time at resonance to be $\tau_{trans} \approx 30 \text{ fs}$. The decay time of the cavity polaritons can be calculated using equation 14. Using a cavity escape time of $\tau_{cav} = 35 \text{ fs}$, we calculate that at resonance, the upper or lower branch polariton states decay with a lifetime of $\mathbf{t}_{u,L}(42.5^\circ) \approx 70 \text{ fs}$ [footnote]. As the transfer time between branches is approximately *half* that of the polariton decay time from either branch, it is apparent that inter-branch transfer process will dominate over radiative decay. In fact, we calculate that approximately 80% of all of the the upper branch polaritons transfer to lower branch states.

The time-scale for the inter-branch transition predicted by our model is $\sim 30 \text{ fs}$. In many molecular systems, both in solution and in the solid state, there are intramolecular vibrational energy redistribution processes that occur over time scales of a few tens of femtoseconds or less [Book]. Thus the inter-branch population transfer proposed here could be thought of being analogous to the ultra-fast relaxation processes that occur through coupled vibrational states

1.7 Photon Emission Following Resonant Excitation

We now review our work on studying the emission from a strongly-coupled organic semiconductor microcavity that has been excited resonantly using a laser [ref]. Under resonant

excitation, photons having energy and in-plane momentum equal to one of the polariton modes are incident on the cavity. These photons can then directly excite a cavity polariton state. In microcavities containing inorganic quantum wells, a number of effects have been studied following resonant excitation, including the temporal dynamics of polariton emission [Sermage, Savona, Norris2], polariton mediated Raman scattering [Fainstain1, Fainstain2, Sasha], polariton relaxation mechanisms [Stanley2] and (bosonic) stimulated scattering [Stevenson, Savvidis].

1.7.1 Resonant Excitation Measurements

We have again explored the properties of strongly-coupled microcavities containing the J-aggregates shown in figure 7(a). The resonant excitation of the microcavities was achieved using a tunable *cw* Ti-sapphire laser. In these experiments, the cavity was placed in a cryostat with wide angular access. Experiments were carried out over the temperature range 60 - 300 K. The experimental setup is shown schematically in the inset of figure 21. Here, the laser is incident on the sample surface at an angle Θ . The energy of the incident laser photons is fixed to the energy of the polariton state *at that angle*. The photon emission is then collected at an angle Φ . Fig. 21(a) shows a series of spectra recorded at $T = 120$ K for excitation at $\Theta = 34^\circ$, and detection at a series of angles between $\Phi = 0^\circ$ to 18° . It can be seen that each spectrum is composed of a relatively broad emission peak, with additional sharp features superimposed at 1.698 and 1.699 eV. The broad emission occurs from radiative-decay of polaritons that have scattered down in energy along the lower branch. We find that the energy of the sharp features are independent of collection angle, with the strongest sharp line occurring at an energy of 73.4 meV below the laser line. Fig. 22 shows a schematic sketch of the experimental methodology. The solid arrows indicate transitions to different states that can be probed by angle-tuning.

To determine the origin of the sharp peaks, spectra were recorded for fixed angles of excitation (Θ) and detection (Φ). However now, the energy of the laser was varied, tuning it through resonance with the lower polariton branch. A series of spectra recorded at $T = 120$ K are presented in Fig. 21(b). As expected the lower polariton branch emission energy is constant, as the angle of detection is fixed. However, the energy of the sharp lines superimposed on the broader PL peak depend strongly on the laser energy. The energy separation between these peaks and the laser is constant with a separation of -73.4 meV below the laser line being found for the strongest line. The laser tuning experiment is represented in the diagram of Fig. 22 by the dashed arrows. The constant energy separation from the laser energy, independent of laser energy and angle of detection, provides strong evidence that the sharp features arise from an inelastic scattering process, namely Raman scattering. It can be seen in the Raman spectra shown in figure 18, that there is indeed a strong Raman line (that originates from a vibrational mode of the cyanine monomer) at 73 meV.

We present further evidence to support the assignment of Raman scattering to the sharp features shown in figure 21(a) and (b) in Fig. 21(c). Here, polariton emission spectra recorded at 300 K are presented, generated under conditions of resonant excitation into the lower polariton branch at $\Theta \approx 0^\circ$ at an energy of 1.707 eV. The polariton emission is now observed at energies up to nearly 80 meV above the excitation energy, due to the large thermal energy of equilibrium polaritons at 300 K. A relatively weak sharp feature is also observed at 1.781 eV, corresponding to an energy of +73.4 meV above the laser energy. This sharp feature arises from anti-Stokes Raman scattering. This process occurs as the phonon population at 300K is sufficient to allow the anti-Stokes companion of the Stokes features observed at lower temperature in Figs 20(a) and (b) to be detected. It is important to note that in contrast to inorganic microcavities where strong

coupling effects are only easily observed at $T < 100$ K due to the small exciton binding energies and Rabi splittings, the polaritons in organic structures are stable at room temperature and above. This high temperature stability permits the observation of the anti-Stokes resonant Raman process for the first time in a strongly coupled microcavity.

1.7.2 The Generation of Raman Emission in a Microcavity

It can be seen from Figs 21(a) and (b), that the Raman intensities are maximised when they are in resonance with the polariton emission peaks. In Fig. 21(a), the excitation is in resonance with the lower polariton branch at 34° . Thus for detection at 10.5° where the Raman intensity is maximum, both incident and scattered photon energies coincide with lower polariton branch states. In this case the double resonance condition is achieved (the thick arrow in the diagram of Fig. 22). Similarly in Fig. 21(b), where the laser energy is tuned, the maximum in Raman intensity is found when both the laser and the scattered photons are resonant with the polariton dispersion curves.

Raman scattering in a microcavity can be thought of as the result of three steps: 1) The transmission of a photon into the sample and conversion to a polariton, 2) phonon-mediated scattering from one polariton state to another, 3) the subsequent propagation and transmission of the scattered polariton and conversion to an external photon. The transmission of a photon into the cavity at any particular angle (1) is maximised when its energy coincides with the energy of a photon-like cavity mode. Similarly in process 3, the escape of a photon from the cavity at any particular angle is also maximised when the energy of the photon coincides with the energy of a photon-like cavity mode. On the basis of this, we can understand the observed energy and angular dependence of the Raman signal: In angle tuning experiments, the energy of the cavity mode (which can be identified by the polariton emission) is tuned through the energy of the Raman scattered photon. The escape of the Raman photons from the cavity is therefore maximised when their energy coincides with the energy of the polariton emission (schematically shown in fig. 22). In energy tuning experiments, both the efficiency of transmission of the photons in and out of the cavity are varied. Again, the Raman scattering efficiency is maximised when the energy of the incident laser and the Raman photon coincide with points on the lower branch.

Control experiments have demonstrated that the Raman scattering efficiency in the microcavities (characterised by a finesse of $Q \approx 50$) under double resonance conditions is about 300 times larger than that for the a non-cavity control sample of J-aggregates in PVA. It has been shown that the enhancement of the Raman efficiency is a strong function of the magnitude of the confined optical field within the cavity, which is itself a function of cavity finesse. High finesse inorganic cavities with $Q \sim 2000$ have been reported to show enhancements up to 10^4 [Fainstain3]. We therefore conclude that our measurements are in good accord with the optical processes that occur in inorganic semiconductor microcavities.

The cavity induced enhancement of Raman scattering is particularly interesting for investigations of non-linear processes. Recent studies of resonant Raman scattering in conjugated polymer thin films have exhibited non-linear character under high power pulsed laser excitation [Shkunov]. The significant enhancements of Raman scattering found in this work therefore suggest interesting opportunities for the investigation of non-linear processes in strongly coupled microcavities [Bradley] using high levels of resonant pulsed laser excitation

1.8 Photon-Mediated Hybridisation between Frenkel Excitons

Recently a number of authors have studied the interaction between different optical and electronic excitations in a microcavity. In the weak-coupling regime, it has been claimed that the optical structure of a microcavity can be used to enhance dipole-dipole interactions [Hopmeier2, Andrew, Ginger]. These observations have yet to be validated theoretically [Basko], and it is clear that more research in this area is needed. However it is clear that modifying electronic processes by control over optical nanostructure would be an attractive and exciting prospect. Coupling between different optical and electronic excitations has also been studied in the strong-coupling regime. Here, the interactions between two inorganic QW exciton states with a single photon state [Wainstain1] two photon states with a single (inorganic) exciton state [Barmy2], and two (inorganic) exciton states interacting with two photon states [Barmy3] have been reported.

In this section, we review our recent work [Lidzey3, Lidzey7] on the fabrication of microcavities containing two different types of organic semiconductor, both of which are strongly coupled to the same cavity mode. As discussed in section 1.5, strong-coupling in a microcavity necessarily implies that the excitonic states within the cavity are all driven coherently by the same optical field. As we will show, simultaneous strong coupling of the individual exciton species to a single cavity-photon mode leads to new eigenmodes that can be described as exciton-photon-exciton admixtures of the three states. One may think of this coupled system in terms of a photon-mediated hybridisation of the two exciton states. This hybridisation therefore *coherently* couples the two different organic semiconductor materials. We will show that such systems are analogous with biological light-harvesting complexes, which are able to mediate long-range energy transfer.

1.8.1 Hybrid Semiconductor Microcavities

To achieve a photon mediated hybridisation between two organic semiconductors, it is necessary to choose a combination of materials, whereby (i) each individual material can strongly-couple to a cavity photon, and (ii) the energy separation (ΔE) between the transitions of the two semiconductors must not be much greater than the Rabi-splitting energy. To achieve these conditions, we have utilised the two cyanine dyes shown in figs 7(a) and (b). For simplicity, we label these materials Ex_1 and Ex_2 . The difference in their peak absorption energy is approximately 60 meV which is comfortably less than the Rabi-splittings of 80 meV that we observe in single component microcavities. The generic structure of the microcavities that we have fabricated is shown in figure 23. The cavity medium between the DBR and the metallic mirror is composed of two J-aggregate films separated by a 100 nm thick layer of the transparent dielectric polymer polystyrene. This ensures that the only coupling that can occur between the two exciton species is that mediated by a cavity photon, as short-range dipole-dipole interactions are characterised by Förster transfer radii of typically less than 10 nm.

Figure 24(a) shows a series of reflectivity spectra measured at increasing viewing angle (spectra are displaced vertically for the sake of clarity). The vertical dotted lines correspond to the peak absorption energy of the Ex_1 and Ex_2 excitons in a non-cavity control film. At 15° , a strong dip can be seen at 1.72 eV, which corresponds to the cavity photon. Two other features are also apparent at 1.79 and 1.87 eV, which correspond to the Ex_1 and Ex_2 exciton-like modes. The energy of three modes as a function of angle is plotted in figure 24(b) with the solid dots being the measured data points. The energy of the uncoupled excitons is shown as horizontal

dotted lines. As in the single component cavity, the polariton branches undergo anti-crossing around the absorption energy of the two different exciton modes.

We describe this system using a model based on the interaction of two excitons and one photon mode, and we write the matrix equation

$$\begin{pmatrix} E^{cav}(k_x) - E & V_1 & V_2 \\ V_1 & E_{Ex1} - E & 0 \\ V_2 & 0 & E_{Ex2} - E \end{pmatrix} \begin{pmatrix} \mathbf{a} \\ \mathbf{b} \\ \mathbf{g} \end{pmatrix} = 0 \quad (35)$$

where E^{cav} , E_{Ex1} and E_{Ex2} are the energies of the non-interacting cavity photon and the two excitons and E are the eigenvalues of the coupled system. V_1 and V_2 are the interaction potentials between the photon and each of the two excitons and α , β and γ are the coefficients that correspond to the bare photon, and the Ex_1 and Ex_2 exciton modes respectively. The same result can be obtained using the macroscopic approach (summarised by equation 20) using a dielectric constant with two different resonances. We therefore write

$$\mathbf{e}(\omega) = \mathbf{e}_o + \frac{f_1}{\omega_1^2 - \omega^2 + i\mathbf{g}} + \frac{f_2}{\omega_2^2 - \omega^2 + i\mathbf{g}} \quad (36)$$

where ω_1 and ω_2 are the frequencies of the two resonances, and f_1 and f_2 are their corresponding oscillator strengths.

However we proceed using equation 35 to describe the energy of the polariton branches. The matrix is diagonalised, and then fit to the experimental data as was demonstrated for a single component cavity. The solid lines in figure 22(b) are the eigenvalues predicted using the coupled oscillator model. Our best fit used values for the exciton energies of $E_{Ex1} = 1.762$ eV, $E_{Ex2} = 1.857$ eV, and predicts Rabi-splittings of $(\hbar/2\pi) \cdot \Omega_{Ex1} = 77.5$ meV, $(\hbar/2\pi) \cdot \Omega_{Ex2} = 78.9$ meV. The exciton energy used in the model varies slightly from the measured values (1.778 eV, 1.842 eV), however such shifts can be explained by the asymmetric linewidths of the J-aggregate excitons [Barmy, Ell]. As the energy separation between the excitons (60 meV) is smaller than the Rabi-splittings between the branches, it is possible for the photon to interact with both exciton modes *simultaneously*, forming a coherent superposition of particles.

Figure 25 shows the eigenvector coefficients used to describe the 3 cavity branches. It can be seen, that the upper and lower polariton branches are mainly composed of a superposition of the cavity photon (α), and either Ex_1 (β) or Ex_2 (γ). However, there is a mixing between all three modes in the central branch, and at 30° the middle branch contains approximately equal amplitudes of the cavity photon and the two exciton species. A hybrid state has thus been created, delocalised throughout the cavity, which is composed of coherently coupled excitons spatially separated by some 100 nm. It is interesting to consider whether it will prove possible to utilise our system as the basis for efficient long-range energy transfer. We can perhaps view the hybrid exciton state supported by this cavity as linking two cavity-polariton states, each of whose excitonic components are widely physically separated. In section 1.6 we demonstrated that the emission intensity from a microcavity containing a single organic semiconductor could be explained using a phonon-mediated energy-transfer process between the upper and lower polariton branches. In this hybrid semiconductor microcavity, a similar energy transfer process between (for example) the upper polariton branch to the lower branch would involve the movement of energy, as the excitonic components associated with these branches are physically

separated. If such a system could be demonstrated, it could, in principle provide a method to move energy via a cavity photon over distances much larger than is permitted by direct dipole-dipole coupling.

It is intriguing to consider whether there are similarities between the phenomena we have been studying and the processes that occur in natural photosynthesis. The observed behaviour of the light-harvesting complex in funneling energy to the reaction centre and the subsequent electron transfer that initiates the energy conversion process pose many intriguing questions. These processes are extremely fast and efficient and are believed to involve coherent excitations of several different molecules [Fleming]. In the light harvesting complex, there are expected to be many energy transfer processes between closely separated and efficiently coupled chromophores before trapping on the reaction centre, yet the overall efficiency is still near unity. In this situation, the Förster dipole-dipole description of energy transfer is expected to be limited because the point dipole approximation breaks down and transfer occurs from excited vibrational levels. In addition, the chromophore units are considered to be strongly-coupled with exciton splittings of ~ 25 meV that are larger than the inhomogeneous linewidths. Short time energy transfer may well then be akin to the scattering processes between coupled exciton levels that are discussed, albeit in a different context, above.

1.9 Future Prospects

In this chapter, I hope that I have communicated some of the interesting features of our research programme on strongly-coupled organic semiconductor microcavities. The interest and novelty of this research area comes in part from the significant difference between the properties of Mott-Wannier excitons, (which have been studied in detail in microcavities), and Frenkel excitons. It is already clear that such differences result in the formation of optical structures that have very different optical properties. So far, we have shown that because of the large oscillator strength of Frenkel excitons, we can achieve strong coupling at room temperature, and can observe ‘giant’ Rabi-splittings. We have also shown that the large binding energy of Frenkel excitons allows the observation of anti-stokes Raman scattering in a microcavity for the first time. We anticipate that there will almost certainly be more new effects waiting to be discovered. Such experimental work will, by necessity, have to be coupled with high level theoretical investigation to allow a full picture of the physics of organic semiconductor microcavities to be developed.

One area that is likely to be particularly promising is the study of stimulated scattering effects. At present, this area is generating considerable excitement in the inorganic semiconductor microcavity community. It has been shown [Stevenson, Savvidis², Saba, Huang, Dang] that under resonant pumping, highly non-linear processes occur. Such effects originate because of the bosonic character of cavity polaritons. At a certain pump power, the number density of a particular polariton state (usually one with zero in plane momentum) can stimulate the scattering of other polaritons into the same state. The strong increase of final state population corresponds to a “condensation” to a polariton mode with macroscopic occupancy, the phenomena possessing a number of similarities to Bose-Einstein condensation. It has been shown [Saba] that the maximum temperature at which such a process will occur is a function of the binding energy of the excitons within the cavity, and thus strongly-coupled organic excitons are likely to display such scattering effects at room temperature. It has been proposed that such structures could find applications as ultra-fast optical switches and amplifiers.

Finally, recent theoretical work has discussed the optical properties of hybrid organic-inorganic structures [Agranovich1, Agranovich2]. It is predicted that a microcavity which contained strongly-coupled Mott-Wannier excitons and Frenkel excitons would allow the creation of hybridised systems, where the characteristics of the organic and inorganic excitons would both in some measure be present in a hybrid-polariton state. Such structures may be of significant importance in creating new types of semiconductor optoelectronic devices and in generating optical structures having enhanced optical non-linearity.

Appendix

Our experimental measurements have demonstrated that organic semiconductor microcavities can show Rabi-splittings at least an order of magnitude larger than those typically found in inorganic semiconductor microcavities. Such enhancements in splitting can be understood using equation 7. The total optical path length in a microcavity (L_{eff}) is given by

$$L_{eff} = L_c + L_{DBR}^{Tot} \quad (A1)$$

where L_c is the distance between the two cavity mirrors, and L_{eff}^{Tot} is the total penetration of the optical field into the cavity DBRs. The optical penetration into a *single* dielectric mirror L_{DBR} is given by

$$L_{DBR} = \frac{\lambda}{4n_c} \frac{n_L n_H}{n_H - n_L} \quad (A2)$$

where λ is the wavelength of the light in the cavity, n_c is the refractive index of the material within the cavity, and n_H (n_L) is the refractive index of the high (low) layers which comprise the dielectric mirror.

In table 1 below, we compare numerically the optical properties of an inorganic microcavity and the organic 4TBPPZn cavity that demonstrated a 160 meV Rabi-splitting.

Parameter	Inorganic III-V QW Cavity	Organic 4TBPPZn Cavity
Cavity structure	20 pair DBR / cavity / 18 pair DBR	9 pair DBR / cavity / Silver
DBR Mirror composition	$Al_xGa_{1-x}As$ ($n_L = 3.08$) $AlAs$ ($n_H = 3.66$)	SiO_2 ($n_L = 1.45$) Si_xN_y ($n_H = 1.95$)
Cavity material and ref. index	GaAs, 3 $In_yGa_{1-y}As$ QWs $n_c = 3.08$	4TBPPZn in PS, $n_c = 1.63$
Penetration in each DBR (L_{DBR})	1.6λ	0.87λ
Cavity path-length (L_c)	λ	$\lambda/2$
Total optical path-length (L_{eff})	4.2λ	1.37λ
Cavity operational wavelength	855 nm	430 nm
Total physical cavity length	1165 nm	360 nm
Rabi-splitting energy	5 meV	160 meV
Oscillator strength per QW	$4.2 \times 10^{12} \text{ cm}^{-2}$	- N / A -
Effective oscillator strength	$1.05 \times 10^{13} \text{ cm}^{-2}$	$\sim 10^{15} \text{ cm}^{-2}$

In Table 1, the effective optical cavity length of the organic microcavity is calculated assuming the penetration of the optical field into the metallic mirror is negligible. The physical length of the cavity is then obtained by dividing the optical cavity length by the cavity refractive index (n_c). The effective oscillator strength of the inorganic QWs used above takes into account that not all of the QWs are located at an antinode of the confined optical field. This reduces the effective oscillator strength of the 3 QWs to $2.52 f_{inorg}$, where f_{inorg} is the oscillator strength of a single QW. The effective oscillator strength of the organic 4TBPPZn layer within the cavity can then be estimated using

$$f_{org} = f_{inorg} \left(\frac{n_{org}^2 L_{eff}^{org}}{n_{inorg}^2 L_{eff}^{inorg}} \right) \left(\frac{\Omega_{org}}{\Omega_{inorg}} \right)^2 \quad (\text{A3})$$

It can be seen from Table 1, that the effective oscillator strength of the material used in the cavity that had a 160 meV splitting is approximately 100 times larger than the effective oscillator strength of 3 III-V QWs. This enhanced oscillator strength is anticipated to increase the Rabi-splitting by a factor of 10 times. An additional enhancement of the Rabi-splitting also arises because the optical field is more effectively concentrated in the region of the organic semiconductor material. In eqn A3, the term describing the spatial extent of the optical field ($n^2 L_{eff}$) is 11 times larger in the inorganic cavity compared to the organic cavity. This occurs because of the low refractive index of the organic semiconductor and because the cavity utilises a metallic mirror in the place of one of the DBRs. The effect of the increase in the optical field in the region of the semiconductor increases the Rabi-splitting by a factor of $\sqrt{11} = 3.3$.